CrossMark

J. Fluid Mech. (2016), *vol.* 801, *pp.* 392–429. © Cambridge University Press 2016
doi:10.1017/jfm.2016.455

Viscoelastic shear flow over a wavy surface

Jacob Page[1] **and Tamer A. Zaki**[1,2,†]

[1]Department of Mechanical Engineering, Imperial College, London SW7 2AZ, UK

[2]Department of Mechanical Engineering, Johns Hopkins University, Baltimore, MD 21218, USA

(Received 7 January 2016; revised 11 May 2016; accepted 1 July 2016;
first published online 25 July 2016)

A small-amplitude sinusoidal surface undulation on the lower wall of Couette flow induces a vorticity perturbation. Using linear analysis, this vorticity field is examined when the fluid is viscoelastic and contrasted to the Newtonian configuration. For strongly elastic Oldroyd-B fluids, the penetration of induced vorticity into the bulk can be classified using two dimensionless quantities: the ratios of (i) the channel depth and of (ii) the shear-waves' critical layer depth to the wavelength of the surface roughness. In the shallow-elastic regime, where the roughness wavelength is larger than the channel depth and the critical layer is outside of the domain, the bulk flow response is a distortion of the tensioned streamlines to match the surface topography, and a constant perturbation vorticity fills the channel. This vorticity is significantly amplified in a thin solvent boundary layer at the upper wall. In the deep-elastic case, the critical layer is far from the wall and the perturbation vorticity decays exponentially with height. In the third, transcritical regime, the critical layer height is within a wavelength of the lower wall and a kinematic amplification mechanism generates vorticity in its vicinity. The analysis is extended to localized, Gaussian wall bumps using Fourier synthesis. The Newtonian flow response consists of a single vortex above the bump. In the shallow-elastic flow, a second vortex with opposite circulation is established upstream of the surface protrusion and is induced by the vorticity layer on the upper wall. In the deep transcritical case, the perturbation field consists of a pair of counter-rotating vortices centred on the large vorticity around the critical layer. The more realistic FENE-P model, which accounts for the finite extensibility of the polymer chains, shows the same qualitative behaviour.

Key words: instability, non-Newtonian flows, viscoelasticity

1. Introduction

The introduction of fluid elasticity can fundamentally modify Newtonian flow dynamics. Some examples include the tendency of the polymer to alter the linear amplification of disturbances in shear flows, shift the onset of laminar-to-turbulence transition and reduce drag in the turbulent flow regime. In order to explain the mechanics underpinning some of these flows, there has been recent focus on the transient evolution of idealized disturbances in viscoelastic fluids in both the linear and nonlinear regimes. In the context of such dynamical studies, an important problem

† Email address for correspondence: t.zaki@jhu.edu

https://doi.org/10.1017/jfm.2016.455 Published online by Cambridge University Press

is receptivity, and in this work we examine the structure of vortical disturbances generated by surface roughness. The problem set-up is analogous to the Newtonian study by Charru & Hinch (2000). We examine the flow response due to small surface undulations on the lower wall of a viscoelastic Couette flow. Our linear analysis demonstrates that elasticity introduces new interesting regimes which differ appreciably from the Newtonian flow.

1.1. *The effect of viscoelasticity on flow stability*

Viscoelasticity has a profound effect on the stability characteristics of inertia-dominated flows. For example, the temporal growth of inviscid instability waves in mixing layers is attenuated by elasticity, and the amplification of short scales can be suppressed entirely (Azaiez & Homsy 1994). In jets, the interplay between fluid elasticity and flow inertia introduces new modes of instability (Rallison & Hinch 1995). Furthermore, spatio-temporal analyses of these flow configurations indicate that viscoelasticity enlarges the region of the parameter space for which these free-shear layers are absolutely unstable (Ray & Zaki 2014, 2015). Some of these effects can be understood through an analogy between the elastic normal stress in the shear layer and a membrane tension.

The influence of fluid elasticity on the stability characteristics of moderate Reynolds number, bounded flows has also received attention. In channels, a small amount of elasticity can stabilize the flow with respect to exponential instabilities (Zhang *et al.* 2013). The effect of viscoelasticity on non-modal, transient amplification processes was investigated by Hoda, Jovanović & Kumar (2008, 2009). Those authors computed the flow response to stochastic body forcing in the momentum equations and demonstrated that the polymer stress fluctuations enhance the associated kinetic energy amplification. In a more recent study, Zhang *et al.* (2013) examined optimal velocity disturbances in channel flows at subcritical Reynolds numbers. A small amount of elasticity strengthens the amplification of streamwise streaks relative to the Newtonian flow, but damps oblique disturbances. The effect of polymer additives on both the lift-up and Orr amplification mechanisms was examined analytically by Page & Zaki (2014, 2015). For high Weissenberg numbers, two-dimensional vortical disturbances amplify as they align favourably with the shear, which was termed a reverse-Orr effect. The nonlinear stages of the transition process in inertia-dominated viscoelastic channel flow were examined by Agarwal, Brandt & Zaki (2014). They performed direct numerical simulations of subcritical transition initiated by a localized velocity disturbance, and demonstrated that the polymer attenuates the streamwise streaks in the nonlinear regime.

In the above studies the base flows under consideration were parallel, with straight streamlines. In those configurations, the influence of the streamline tension due to the polymer was often stabilizing. In curved geometries, streamline tension has an opposite effect and introduces new elastic instabilities. The most striking feature of these instabilities is their persistence in inertialess flows (Shaqfeh 1996). A combination of experiments and linear stability analyses of an inertialess Taylor–Couette flow identified their physical origin (Muller, Larson & Shaqfeh 1989; Larson, Shaqfeh & Muller 1990; Shaqfeh, Muller & Larson 1992). The viscoelastic inertialess instability depends on the shear rate (Larson *et al.* 1990), and draws energy from the base-state hoop stress in the curved streamlines. A succession of curvature-induced purely elastic instabilities can give way to elastic turbulence – a chaotic state with a broad range of spatial and temporal scales (Groisman & Steinberg 2000).

https://doi.org/10.1017/jfm.2016.455 Published online by Cambridge University Press

While there is no inertialess instability in planar viscoelastic Couette flow (Gorodtsov & Leonov 1967; Renardy & Renardy 1986), parallel viscoelastic flows can exhibit strong non-modal amplification in the zero-Reynolds-number limit (Jovanovic & Kumar 2010, 2011; Lieu, Jovanović & Kumar 2013; Page & Zaki 2014). In addition, although these flows are asymptotically stable to infinitesimal perturbations, they may be unstable to finite-amplitude disturbances (Morozov & Saarloos 2007). These perturbations induce finite curvature in the streamlines and the flow becomes susceptible to a secondary linear instability (Meulenbroek *et al.* 2004; Morozov & Saarloos 2005). There is also experimental evidence that a planar viscoelastic flow can support a self-sustaining chaotic state (Pan *et al.* 2013).

The present study is focused on the manner by which wall undulations induce streamline curvature in parallel viscoelastic shear flows. In low-Reynolds-number Newtonian configurations the flow field is determined by the instantaneous diffusion of vorticity (Charru & Hinch 2000). As will be demonstrated, the viscoelastic case is richer due to the potential role of the base-state stresses and the wave-like behaviour of vorticity.

1.2. *Vorticity wave propagation in viscoelastic fluids*

At finite Reynolds numbers the phase difference between the flow and polymer responses provides a mechanism for the propagation of vorticity waves (Joseph 1990). This phenomenon is apparent in the viscoelastic analogues to some of the classical time-dependent solutions of the Navier–Stokes equations. For example, in the starting plate, or Stokes' first problem, the vortex sheet initiated by the jump in the wall velocity propagates upwards as a shear wave (Tanner 1962; Denn & Porteous 1971). In oscillatory pipe flows, shear waves can lead to instability (Torralba *et al.* 2007; Casanellas & Ortín 2014). In micellar solutions, their interference can initiate the formation of shear bands (Zhou, Cook & McKinley 2012). In wall-bounded flows, vorticity wave propagation and reflection can result in spanwise-travelling re-energizing streaks (Page & Zaki 2014).

The highly tensioned streamlines in a viscoelastic shear flow provide an additional mechanism for wave propagation along the flow direction. Unlike the aforementioned shear waves, these streamwise-travelling waves persist even in dilute solutions. They can lead to new instabilities in flows with shear discontinuities (Rallison & Hinch 1995), and the combined effects of wave propagation and shear deformation can amplify disturbances as they align with the shear (Page & Zaki 2015). More fundamentally, the propagation of vorticity waves along tensioned streamlines can introduce critical layers in the flow. Across these layers, the domain is divided into 'subcritical' and 'supercritical' regions where the fluid is travelling slower and faster than the wave speed, respectively (Joseph, Renardy & Saut 1985). Yoo & Joseph (1985) and Ahrens, Yoo & Joseph (1987) have investigated the change of type which occurs for upper convected Maxwell fluids in channels and pipes with surface waviness. Close to the wall, the vorticity equation is elliptic. There is a sudden change of type at the critical layer, and in the supercritical core of the flow domain the vorticity equation is hyperbolic. This critical layer is smoothed in fluids with a finite solvent viscosity, which are the focus of the current work. However, the critical layers can still have a dramatic influence on the penetration and amplification of vorticity generated at the wavy wall.

The studies by Yoo & Joseph (1985) and Ahrens *et al.* (1987) focused on the phenomenon of a change in type which occurs in inertia-dominated, instantaneously elastic flows – although they also commented on the form of the perturbation field.

https://doi.org/10.1017/jfm.2016.455 Published online by Cambridge University Press

For example, Yoo & Joseph (1985) noted that the spanwise-vorticity perturbations induced by the wavy wall are 'swept out along characteristics' in the hyperbolic core of the channel, although they could not find an explanation for this property. In the present study, the structure of the vorticity field is explained in detail in terms of the coupling between vorticity and the polymer torque. Detailed asymptotic analyses identify the mechanism for vorticity amplification at the critical layer. Furthermore, we find intriguing behaviour in inertialess flows where the critical layer is outside of the flow domain and does not influence vorticity penetration. The competing effects of the wall wavelength, channel depth, critical layer height, inertia and fluid elasticity are distilled to a dependence on just two parameters: the ratios of the channel depth and of the critical layer height to the roughness wavelength.

The remainder of this paper is organized as follows: in § 2 the physical problem is defined, and the linear perturbation equations are manipulated into a vorticity/polymer-torque system. The various flow regimes are identified and parameterized using a phase diagram in § 3, before the underlying mechanics are explained in § 4. The flow response to localized wall roughness is examined in § 5 and conclusions are provided in § 6.

2. Theoretical formulation

On a macroscopic scale, the presence of small amounts of polymer dissolved in a solvent results in an additional forcing term in the momentum equation due to a polymeric stress, $\mu_p F_i^* = \mu_p \partial T_{ij}^*/\partial x_j^*$. The modified flow equations are

$$\frac{\partial U_i^*}{\partial x_i^*} = 0, \tag{2.1a}$$

$$\rho\left(\frac{\partial U_i^*}{\partial t^*} + U_j^*\frac{\partial U_i^*}{\partial x_j^*}\right) = -\frac{\partial P^*}{\partial x_i^*} + \mu_s\frac{\partial^2 U_i^*}{\partial x_j^*\partial x_j^*} + \mu_p F_i^*, \tag{2.1b}$$

where the asterisk indicates a dimensional variable. The quantities μ_s and μ_p are the dynamic solvent and polymer viscosities, respectively. The current study focuses on dilute solutions, which can be described by the Oldroyd-B model. In an Oldroyd-B fluid, polymer chains are modelled as infinitely extensible dumbbells, and stress is related to the polymer conformation by $T_{ij}^* = (1/\varsigma)(C_{ij} - \delta_{ij})$, where ς is the polymer relaxation time. The polymer conformation evolves according to

$$\frac{\partial C_{ij}}{\partial t^*} + U_k^*\frac{\partial C_{ij}}{\partial x_k^*} = C_{ik}\frac{\partial U_j^*}{\partial x_k^*} + C_{jk}\frac{\partial U_i^*}{\partial x_k^*} - T_{ij}^*. \tag{2.1c}$$

The Oldroyd-B model predicts some of the important behaviours associated with viscoelastic fluids, for example the normal stress difference in shear flows and a fading memory of flow history. In this work, we exploit its simplicity to examine analytically the influence of these effects on the vorticity induced by surface waviness in Couette flow. However, the Oldroyd-B model suffers from well-documented deficiencies, in particular its performance at higher shear rates and failure in extensional flows (Bird, Armstrong & Hassager 1987). Therefore, in § 5.2, the more realistic FENE-P model, which accounts for the finite extensibility of the polymer chains, is considered numerically.

https://doi.org/10.1017/jfm.2016.455 Published online by Cambridge University Press

2.1. *The physical problem*

The flow configuration is presented schematically in figure 1. We consider a channel of depth d with flow driven by motion of the top plate at speed U_0. The lower wall has a wavy surface, $y^* = h^*\cos(k^*x^*)$. Under the assumption of small wave slopes, $\varepsilon h \equiv k^*h^* \ll 1$, the flow induced by the surface undulations can be treated as a small $O(\varepsilon)$ perturbation to a Couette base state,

$$U^* = \dot{\gamma}^* y^*, \tag{2.2a}$$

which has an associated constant polymer stress tensor,

$$\boldsymbol{T}^* = \begin{pmatrix} 2\dot{\gamma}^{*2}\varsigma & \dot{\gamma}^* & 0 \\ \dot{\gamma}^* & 0 & 0 \\ 0 & 0 & 0 \end{pmatrix}, \tag{2.2b}$$

where $\dot{\gamma}^* \equiv U_0/d$ is the shear rate. We consider the problem in a frame where the lower wall is at rest and therefore the perturbations appear steady.

The linearized no-slip condition on the undulating lower wall becomes a slip condition on the perturbation velocity,

$$u^*(x^*, 0) = -\dot{\gamma}^* h^* \cos(k^*x^*), \quad v^*(x^*, 0) = 0, \tag{2.3a}$$

while the perturbation velocities vanish at the upper wall,

$$u^*(x^*, d) = v^*(x^*, d) = 0. \tag{2.3b}$$

The problem is non-dimensionalized by the wavenumber, k^*, and the shear rate, $\dot{\gamma}^*$. With this scaling, the base-state velocity profile is $U = \dot{\gamma} y$, with associated non-dimensional base-state stresses $T_{11} = 2W\dot{\gamma}^2$ and $T_{12} = \dot{\gamma}$, where $W \equiv \dot{\gamma}^*\varsigma$ is the Weisenberg number, the ratio of the polymer relaxation time to a flow time scale, and the unit dimensionless shear rate $\dot{\gamma}$ is retained for clarity. The equations governing the linear perturbations are now introduced, and are reduced to an Orr–Sommerfeld equation for the streamfunction and an equation for a quantity that plays the role of a polymer potential.

2.2. *Linear perturbation equations: streamfunction and polymer potential*

For Oldroyd-B fluids, the non-dimensional, steady perturbation equations are

$$\frac{\partial u_i'}{\partial x_i} = 0, \tag{2.4a}$$

$$\Gamma_{jk}x_k\frac{\partial u_i'}{\partial x_j} + u_j'\Gamma_{ij} = -\frac{\partial p'}{\partial x_i} + \frac{\alpha^2}{R}\left(\beta\frac{\partial^2 u_i'}{\partial x_j\partial x_j} + (1-\beta)f_i'\right), \tag{2.4b}$$

$$\Gamma_{jk}x_k\frac{\partial f_i'}{\partial x_j} + \frac{1}{W}f_i' = f_j'\Gamma_{ij} + T_{jk}\frac{\partial^2 u_i'}{\partial x_j\partial x_k} + \frac{1}{W}\frac{\partial^2 u_i'}{\partial x_j\partial x_j}, \tag{2.4c}$$

where Γ_{ij} is the base-state velocity gradient tensor. For Couette flow, the only non-zero entry is $\Gamma_{12} = \dot{\gamma}(= 1)$. The quantity $\alpha \equiv k^*d$ is the normalized channel depth, $R \equiv \dot{\gamma}^*d^2/\nu$ is the bulk Reynolds number and $\beta \equiv \nu_s/\nu$ is the ratio of the solvent to total viscosity. The variable $\boldsymbol{f}' \equiv \boldsymbol{\nabla}\cdot\tau'$ is the perturbation force due to the polymer (Page & Zaki 2015).

https://doi.org/10.1017/jfm.2016.455 Published online by Cambridge University Press

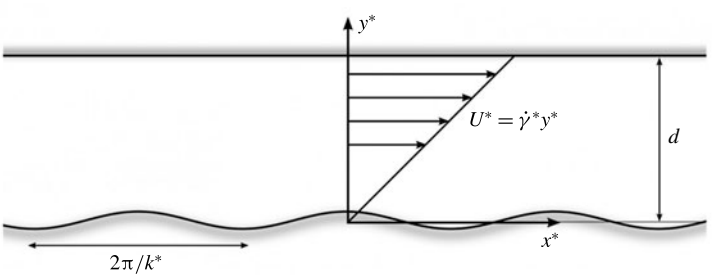


FIGURE 1. Viscoelastic Couette flow over a wavy wall. The unit length is the inverse wall wavenumber k^{*-1}; the unit time is the inverse shear rate $\dot{\gamma}^{*-1}$.

Taking the divergence of (2.4*c*), we find that the polymer force field is solenoidal, $\boldsymbol{\nabla} \cdot \boldsymbol{f}' = 0$. The present focus on two-dimensional perturbations thus motivates the introduction of the pair of vector potentials for the velocity and polymer force fields,

$$\boldsymbol{u}' = \boldsymbol{\nabla} \wedge \psi' \boldsymbol{e}_z, \quad \boldsymbol{f}' = \boldsymbol{\nabla} \wedge \varphi' \boldsymbol{e}_z, \tag{2.5a,b}$$

where ψ' is the perturbation streamfunction and φ' is termed the 'polymer potential', which is instantaneously tangent to the polymer force vectors (Page & Zaki 2015).

We seek solutions of the form

$$\begin{pmatrix} \psi'(\boldsymbol{x}) \\ \varphi'(\boldsymbol{x}) \end{pmatrix} = \mathrm{Re}\left\{ \begin{pmatrix} \psi(y) \\ \varphi(y) \end{pmatrix} \mathrm{e}^{\mathrm{i}kx} \right\}, \tag{2.6}$$

where the unit non-dimensional wavenumber, $k = 1$, is retained for clarity, and manipulate equations (2.4) into a viscoelastic Orr–Sommerfeld system,

$$\mathrm{i}k\dot{\gamma} y \left(\frac{\mathrm{d}^2}{\mathrm{d}y^2} - k^2 \right) \psi = \frac{\alpha^2}{R} \left[\beta \left(\frac{\mathrm{d}^2}{\mathrm{d}y^2} - k^2 \right)^2 \psi + (1-\beta) \left(\frac{\mathrm{d}^2}{\mathrm{d}y^2} - k^2 \right) \varphi \right], \tag{2.7a}$$

$$\mathrm{i}k\dot{\gamma} y \varphi + \frac{1}{W}\varphi = \left[-k^2 T_{11} + 2\mathrm{i}k T_{12} \frac{\mathrm{d}}{\mathrm{d}y} + \frac{1}{W} \left(\frac{\mathrm{d}^2}{\mathrm{d}y^2} - k^2 \right) \right] \psi. \tag{2.7b}$$

The disturbance velocity boundary conditions (2.3*a*) are expressed in terms of the streamfunction,

$$\mathrm{d}_y \psi(0) = -\dot{\gamma} h, \quad \psi(0) = 0, \tag{2.8a,b}$$

where $h = 1$ is assumed such that the wave slope is a small parameter, $\varepsilon h = k^* h^*$. The streamfunction and its gradient have homogeneous boundary conditions at the top wall, $y = \alpha$.

It will often be instructive to analyse the perturbation field in terms of the spanwise vorticity, $\omega \equiv -\nabla^2 \psi = -(\mathrm{d}_y^2 - k^2)\psi$, and the spanwise polymer torque, $\chi \equiv -\nabla^2 \varphi = -(\mathrm{d}_y^2 - k^2)\varphi$, which are governed by

$$\mathrm{i}k\dot{\gamma} y \omega = \frac{\alpha^2}{R} \left[\beta \left(\frac{\mathrm{d}^2}{\mathrm{d}y^2} - k^2 \right) \omega + (1-\beta)\chi \right], \tag{2.9a}$$

$$\mathrm{i}k\dot{\gamma} y \chi + \frac{1}{W}\chi = 2\mathrm{i}k\dot{\gamma} \frac{\mathrm{d}\varphi}{\mathrm{d}y} + \left[-k^2 T_{11} + 2\mathrm{i}k T_{12} \frac{\mathrm{d}}{\mathrm{d}y} + \frac{1}{W} \left(\frac{\mathrm{d}^2}{\mathrm{d}y^2} - k^2 \right) \right] \omega. \tag{2.9b}$$

The polymer torque is proportional to the torque exerted on a fluid element by the polymer stresses.

https://doi.org/10.1017/jfm.2016.455 Published online by Cambridge University Press

3. Flow regimes and phase diagram

3.1. *Quasi-Newtonian flow*

Here we briefly examine the flow response to the surface waviness in the low-Weissenberg-number limit. This limit yields a quasi-Newtonian behaviour, and at leading order, the results are identical to those presented by Charru & Hinch (2000). Therefore, this section establishes the background against which the elasticity-dominated flows are compared in subsequent sections.

In the limit of small Weissenberg number, $W \ll 1$, the polymer behaves like an additional solvent. To leading order in W, the equations for the vorticity (2.9*a*) and polymer torque (2.9*b*) are

$$\mathrm{i}k\dot{\gamma} y\omega_0 = \frac{\alpha^2}{R}\left[\beta\left(\frac{\mathrm{d}^2}{\mathrm{d}y^2} - k^2\right)\omega_0 + (1-\beta)\chi_0\right], \tag{3.1a}$$

$$\chi_0 = \left(\frac{\mathrm{d}^2}{\mathrm{d}y^2} - k^2\right)\omega_0. \tag{3.1b}$$

As anticipated, the polymer torque (3.1*b*) is instantaneously responsive to the flow and, since the background stresses are weak, χ_0 depends on the curvature in the vorticity field alone. The Newtonian spanwise vorticity is recovered after combining the system (3.1),

$$\mathrm{i}k\dot{\gamma} y\omega_0 = \frac{\alpha^2}{R}\left(\frac{\mathrm{d}^2}{\mathrm{d}y^2} - k^2\right)\omega_0. \tag{3.2}$$

An identical equation is obtained in the limit of pure solvent, $\beta = 1$.

The solution to equation (3.2) above a wavy wall was discussed in detail by Charru & Hinch (2000). Those authors demonstrated that the vorticity perturbations induced by the lower wall can be classified into three regimes, depending on the values of a pair of parameters:

$$\alpha \equiv k^* d \quad \text{and} \quad \theta \equiv \left(\frac{\alpha^2}{R}\right)^{1/3} = \left(\frac{\nu k^{*2}}{\dot{\gamma}^*}\right)^{1/3}. \tag{3.3a,b}$$

The first of these, α, is the normalized channel depth. The second, θ, is a normalized viscous length scale. Three regimes are defined following the analysis and terminology introduced by Charru & Hinch (2000): (i) the shallow-viscous regime, $\alpha < 1$; $\theta > \alpha$; (ii) the deep-viscous regime, $\alpha > 1$, $\theta > 1$; (iii) the inviscid regime, $\alpha > 1$, $\theta < 1$.

The vorticity and streamfunction in three examples representative of the Newtonian regimes are reported in figure 2. In figure 2(*a*) the vorticity perturbation fills the channel and the effects of inertia, which would tip the roll structures forward with the shear, are negligible. This behaviour is characteristic of the shallow-viscous regime where the roughness wavelength is longer than the channel depth, $\alpha < 1$, and the viscous length is greater than the channel height, $\theta > \alpha$. In figure 2(*b*), the vorticity perturbations penetrate about a wavelength into the flow and inertial effects are still unimportant. This behaviour, which occurs for deep channels, $\alpha > 1$, with $\theta > 1$, is termed the 'deep-viscous' regime. Finally, figure 2(*c*) is an example of the 'inviscid regime'. The induced rolls are tipped forward under the action of the shear, while the vorticity penetration depth is of the order of the viscous length. This regime is associated with conditions where $\alpha > 1$ and $\theta < 1$.

In order to quantify vorticity penetration, Charru & Hinch (2000) introduced a measure of penetration depth based on the inverse wall vorticity, $|\omega(0)|^{-1}$.

https://doi.org/10.1017/jfm.2016.455 Published online by Cambridge University Press

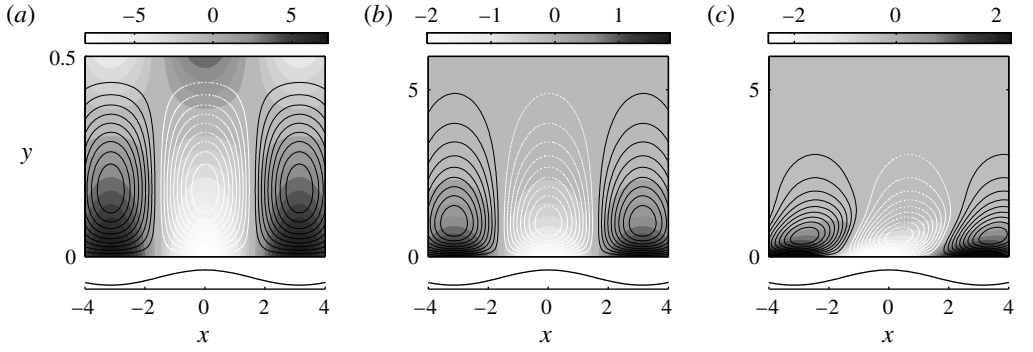


FIGURE 2. Vortical perturbations (top) induced by the wavy wall (bottom) in Newtonian fluids. Filled contours are the spanwise vorticity, lines are the streamfunction. (*a*) Shallow-viscous regime $\alpha = 0.5$ and $\theta = 0.63$. (*b*) Deep-viscous regime, $\alpha = 10$ and $\theta = 4.64$. (*c*) Inviscid regime, $\alpha = 10$ and $\theta = 0.46$.

This definition is intuitive because the action of viscous diffusion means that the vorticity maximum is always at the lower wall, and in deep channels vorticity monotonically decays with increasing y. Elasticity-dominated flows with $W > 1$ do not share these Newtonian characteristics, and a more general definition of penetration depth will be required.

3.2. *Viscoelastic phase diagram*

Similar to the quasi-Newtonian limit, the solution at moderate to high Weissenberg numbers depends on two dimensionless parameters. The first remains the normalized channel depth, $\alpha \equiv k^* d$. However, the viscous diffusion length is now of secondary importance. We will see that vorticity penetration is instead dependent on the parameter,

$$\Sigma \equiv \frac{\sqrt{\mu_p T_{11}^*/\rho}}{\dot{\gamma}^*/k^*}, \tag{3.4a}$$

$$= \frac{\sqrt{2\nu_p \varsigma}}{1/k^*}, \tag{3.4b}$$

which is related to the bulk elasticity, $E^* \equiv (1-\beta)W/R$, by $\Sigma = k^* d\sqrt{E^*}$. However, when written in the form (3.4*a*), Σ may be interpreted as the ratio of a vorticity wave speed, $c_\omega^* = \sqrt{\mu_p T_{11}^*/\rho}$, to the base-flow velocity one wavelength above the lower wall. This classification reflects that vorticity fluctuations in a viscoelastic flow may propagate as streamwise-travelling waves along the tensioned mean-flow streamlines – a scenario which shares some similarities with the propagation of Alfvén waves along magnetic field lines (Chandrasekhar 1961). The difference in the viscoelastic case is that a mean shear is required to establish the normal stress $\mu_p T_{11}^*$, and this shearing also has associated with it a kinematic vorticity amplification mechanism (Page & Zaki 2015). When written in the form (3.4*b*), Σ is a ratio of length scales: the critical layer height and the roughness wavelength. The critical layer is the surface where the speed of the base flow matches the wave speed c_ω^*. While the vorticity perturbations are steady in the present problem, the longitudinal vorticity wave speed c_ω^* remains

https://doi.org/10.1017/jfm.2016.455 Published online by Cambridge University Press

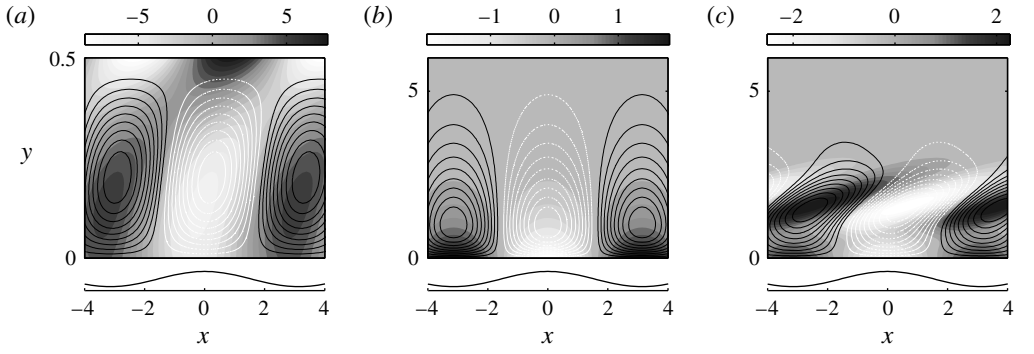


FIGURE 3. Vortical perturbations (top) induced by the wavy wall (bottom). Filled contours are the spanwise vorticity, lines are the streamfunction. (*a*) Shallow-elastic regime $\alpha = 0.5$ and $\Sigma = 3$ with $R = 1$, $\beta = 0.7$, $W = 60$. (*b*) Deep-elastic regime, $\alpha = 10$ and $\Sigma = 60$ with $R = 1$, $\beta = 0.7$, $W = 60$. (*c*) Transcritical regime, $\alpha = 10$ and $\Sigma = 1.9$ with $R = 1000$, $\beta = 0.7$, $W = 60$.

an important property of the viscolelastic flow. The critical layer height, which can be thought of as the point where an observer travelling with the mean flow would see the lower wall disturbance sweep by at the elastic wave speed, has particular physical significance (§ 4.3).

Three examples of vortical disturbances induced by the lower wall in flows with a fairly large Weissenberg number, $W = 60$, are reported in figure 3. The same behaviour is preserved at lower values of W, but a relatively high value was adopted here in order to highlight the observed effects. Each of the panels in the figure illustrates a different regime.

In figure 3(*a*) counter-rotating rolls fill the channel. Rolls with positive vorticity sit above troughs and with negative vorticity over peaks. The parameters correspond to the shallow-viscous behaviour in a Newtonian fluid. However, in this high-Weissenberg-number flow, the rolls are tipped forward, a behaviour normally attributed to inertial effects. In addition, the vorticity maxima are located along the top wall. In general, these characteristics are associated with conditions where $\alpha \lesssim 1$, $\Sigma > \alpha$ which we term 'shallow-elastic' flows.

In figure 3(*b*), the rolls remain in phase with the surface waviness and their associated vorticity decays within roughly one wavelength from the wall. Despite the high Weissenberg number, the perturbation flow is indistinguishable from the Newtonian deep-viscous regime. In general, this behaviour occurs when $\alpha \gtrsim 1$ and $\Sigma \gtrsim 1$, and is denoted the 'deep-elastic' regime.

Finally, the most intriguing behaviour is encountered when $\alpha > \Sigma$ and $\Sigma \lesssim 1$, and is displayed in figure 3(*c*). The vorticity is amplified in stripes tilted forward with the shear, and the amplification is localized around a y-location away from the wall. This regime is referred to as 'transcritical' flow.

Both the shallow-elastic and transcritical flows have characteristics which differ substantially from the Newtonian configuration. Shallow-elastic flows exhibit vorticity amplification at the upper wall, while flows in the transcritical regime are characterized by non-local vorticity amplification in the bulk of the channel. These features motivate a definition of penetration depth based on a measure of the total perturbation vorticity, rather than one constructed from local information about

https://doi.org/10.1017/jfm.2016.455 Published online by Cambridge University Press

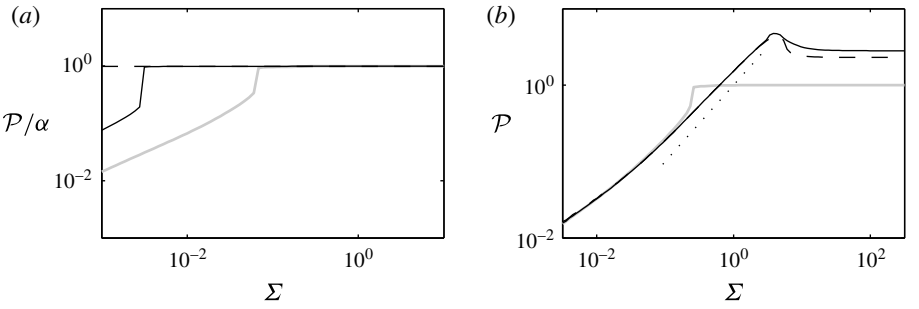


FIGURE 4. Penetration depth, $\mathcal{P}$ as a function of Σ. (*a*) 'Shallow' channels with $W = 60$, $\beta = 0.7$: dashed line, $\alpha = 0.01$; black solid line, $\alpha = 0.1$; grey solid line, $\alpha = 0.5$. (*b*) 'Deep' channels with $W = 60$, $\beta = 0.7$; grey solid line, $\alpha = 1$; black solid line, $\alpha = 5$; dashed line, $\alpha = 10$. The dotted line is $\mathcal{P} = \Sigma$.

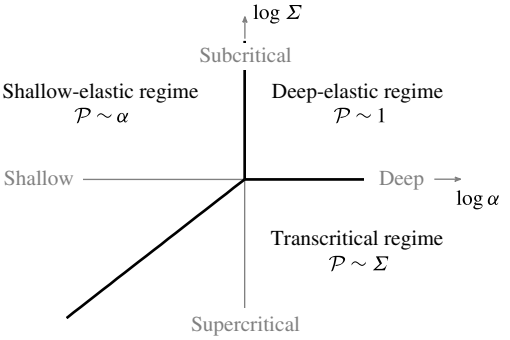


FIGURE 5. Phase diagram for vorticity disturbances initiated by the surface waviness.

the vorticity magnitude. We adopt the following measure of penetration depth,

$$\mathcal{P} \equiv y(\Lambda^r = 0.99); \quad \text{where } \Lambda^r(y) = \frac{\displaystyle\int_0^y |\omega(y')|^2 \, \mathrm{d}y'}{\displaystyle\int_0^\alpha |\omega(y')|^2 \, \mathrm{d}y'}, \tag{3.5}$$

which can account for non-local effects. Note that (3.5) recovers the Newtonian scalings for penetration depth found by Charru & Hinch (2000) in the limit $W \ll 1$.

The penetration depth $\mathcal{P}$ is evaluated for a range of α and Σ and is used in figure 4 to examine the transitions between the three regimes reported in figure 3. Shallow channels, $\alpha < 1$, are considered in figure 4(*a*) and Σ (or the vorticity wave speed) is varied by changing the bulk Reynolds number, R. When the critical layer is outside of the flow domain, $\Sigma \gtrsim \alpha$, the vorticity perturbation fills the channel, $\mathcal{P} \sim \alpha$. Deep channels are considered in figure 4(*b*). When $\Sigma \lesssim 1$ the penetration depth scales with the dimensionless critical layer height, $\mathcal{P} \sim \Sigma$ (transcritical regime). There is a sharp transition to the deep-elastic regime when $\Sigma \gtrsim 1$ and penetration is of the order of a wavelength, $\mathcal{P} \sim 1$.

In analogy to the Newtonian problem (Charru & Hinch 2000), these results may be summarized in the form of a 'phase diagram'. The diagram for the viscoelastic Couette flow is presented schematically in figure 5. Each of the three regimes

https://doi.org/10.1017/jfm.2016.455 Published online by Cambridge University Press

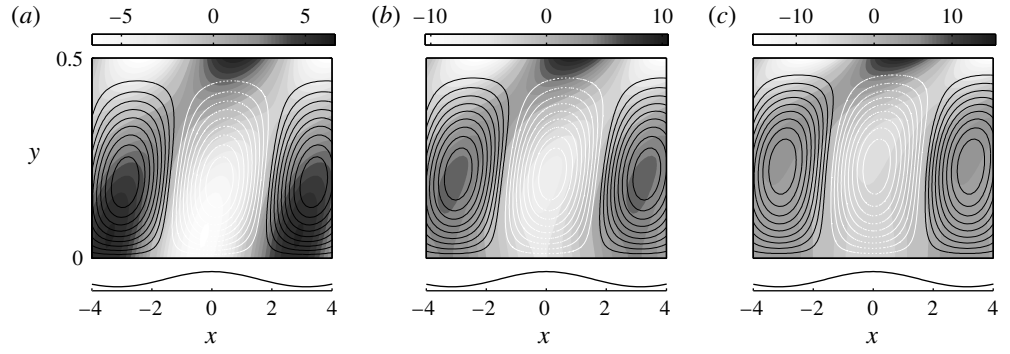


FIGURE 6. Vortical perturbations (top) induced by the wavy wall (bottom) in the shallow-elastic regime. Filled contours are the spanwise vorticity, lines are the streamfunction. The channel depth $\alpha = 0.5$, and the solvent viscosity and bulk Reynolds numbers are fixed, $R = 1$, $\beta = 0.5$. (*a*) $W = 20$ ($\Sigma = 2.24$); (*b*) $W = 40$ ($\Sigma = 3.16$); (*c*) $W = 80$ ($\Sigma = 4.47$).

spans a sector in the $\{\log \alpha, \log \Sigma\}$ plane. This classification does not explain the characteristics of the vorticity eigenfunctions in each regime; for example the vorticity generation at the top wall in shallow-elastic flows or the amplification of vorticity in the bulk fluid in transcritical channels. These effects are now explored further using asymptotic analyses.

4. Asymptotic solutions in the three regimes

4.1. *Shallow-elastic flow*

Shallow-elastic flows are those where $\alpha \lesssim 1$ and $\Sigma > \alpha$. The second of these criteria means that the base flow is slower than the vorticity wave speed; the critical layer is outside of the flow domain. Examples of the streamfunction and vorticity in this regime are provided in figure 6 for increasing values of the Weissenberg number, W. As W is increased, the vorticity across the bulk of the channel becomes nearly constant, except for a rapid variation close to the upper wall where it is significantly amplified. This behaviour should be contrasted with Newtonian shallow-viscous flows where the vorticity distribution is linear and dictated by viscous diffusion.

In order to explain the structure of the vorticity perturbation in this regime, we examine the streamfunction–polymer potential system (2.7) in the long-wave limit, $\alpha \ll 1$. The solution to the long-wave equations will be shown to depend on the parameter $\mathcal{W} \equiv \alpha \dot{\gamma} W$. In the limit $\mathcal{W} \gg 1$ the bulk flow response to the vorticity injection at the bottom wall can be classified as 'elastic', and a solvent boundary layer forms at the upper wall where the spanwise vorticity is amplified by a factor which we will show is $\mathcal{W}^{1/2}$.

The present interest in shallow channels motivates rescaling the equations by the channel height $Y = y/\alpha$, with $\alpha^2 \hat{\psi}(Y) = \psi(y)$, $\hat{\varphi}(Y) = \varphi(y)$. The system of (2.7) becomes

$$\mathrm{i}\alpha\dot{\gamma} Y \left(\frac{\mathrm{d}^2}{\mathrm{d}Y^2} - \alpha^2\right)\hat{\psi} = \frac{\beta}{R}\left(\frac{\mathrm{d}^2}{\mathrm{d}Y^2} - \alpha^2\right)^2 \hat{\psi} + \frac{(1-\beta)}{R}\left(\frac{\mathrm{d}^2}{\mathrm{d}Y^2} - \alpha^2\right)\hat{\varphi}, \quad (4.1a)$$

$$\left(Y + \frac{1}{\mathrm{i}\mathcal{W}}\right)\hat{\varphi} = \left[2\mathrm{i}\mathcal{W} + 2\frac{\mathrm{d}}{\mathrm{d}Y} + \frac{1}{\mathrm{i}\mathcal{W}}\left(\frac{\mathrm{d}^2}{\mathrm{d}Y^2} - \alpha^2\right)\right]\hat{\psi}, \quad (4.1b)$$

https://doi.org/10.1017/jfm.2016.455 Published online by Cambridge University Press

where $\mathcal{W} \equiv \alpha\dot{\gamma}W = U_0\varsigma k^*$ is proportional to the number of bottom waves that an observer travelling at the top wall speed would pass in a relaxation time ς. Assuming that $\alpha \ll 1$, an expansion in powers of α^{-1} yields the leading-order equations,

$$0 = \beta\frac{\mathrm{d}^4\hat{\psi}_0}{\mathrm{d}Y^4} + (1-\beta)\frac{\mathrm{d}^2\hat{\varphi}_0}{\mathrm{d}Y^2}, \tag{4.2a}$$

$$\left(Y + \frac{1}{\mathrm{i}\mathcal{W}}\right)\hat{\varphi}_0 = \left(2\mathrm{i}\mathcal{W} + 2\frac{\mathrm{d}}{\mathrm{d}Y} + \frac{1}{\mathrm{i}\mathcal{W}}\frac{\mathrm{d}^2}{\mathrm{d}Y^2}\right)\hat{\psi}_0. \tag{4.2b}$$

An exact solution to this inertialess system of equations is

$$\begin{aligned}\hat{\psi}_0(Y) \;=\; & C_1Y^2 + C_2Y \\ & + C_3\left(Y + \frac{1}{\mathrm{i}\mathcal{W}\beta}\right)^{(3\beta-2)/2\beta}\mathcal{H}^{(1)}_{(3\beta-2)/\beta}\left(2(1+\mathrm{i})\sqrt{\mathcal{W}\frac{(1-\beta)}{\beta}\left(Y + \frac{1}{\mathrm{i}\mathcal{W}\beta}\right)}\right) \\ & + C_4\left(Y + \frac{1}{\mathrm{i}\mathcal{W}\beta}\right)^{(3\beta-2)/2\beta}\mathcal{H}^{(2)}_{(3\beta-2)/\beta}\left(2(1+\mathrm{i})\sqrt{\mathcal{W}\frac{(1-\beta)}{\beta}\left(Y + \frac{1}{\mathrm{i}\mathcal{W}\beta}\right)}\right),\end{aligned} \tag{4.3}$$

where the $\mathcal{H}^{(j)}_n$ are Hankel functions of order n. The solution is a function of $\mathcal{W}$ and the polymer concentration, β. However, extracting the physical mechanism behind the vorticity amplification from this solution is difficult. Since the upper wall amplification is increasingly pronounced for large $\mathcal{W}$, we instead seek an approximate solution of the long-wave equations (4.2) assuming $\mathcal{W} \gg 1$.

Bulk elastic solution: defining $\varepsilon \equiv \mathcal{W}^{-1} \ll 1$ and $\hat{\Phi}_0 = \varepsilon\hat{\varphi}_0$, equations (4.2) become

$$0 = \varepsilon\beta\frac{\mathrm{d}^4\hat{\psi}_0}{\mathrm{d}Y^4} + (1-\beta)\frac{\mathrm{d}^2\hat{\Phi}_0}{\mathrm{d}Y^2}, \tag{4.4a}$$

$$(Y - \mathrm{i}\varepsilon)\hat{\Phi}_0 = \left(\underbrace{2\mathrm{i}}\; + \underbrace{2\varepsilon\frac{\mathrm{d}}{\mathrm{d}Y}} - \mathrm{i}\varepsilon^2\frac{\mathrm{d}^2}{\mathrm{d}Y^2}\right)\hat{\psi}_0, \tag{4.4b}$$

where the underbraces in the polymer potential equation (4.4*b*) identify the terms associated with the base-state polymer stresses, T_{11} and T_{12} (cf. equation 2.7*b*). We adopt the asymptotic expansion

$$\hat{\psi}_0(Y;\,\varepsilon) \;= \hat{\psi}_0^0(Y) + \varepsilon^{1/2}\hat{\psi}_0^{1/2}(Y) + \varepsilon\hat{\psi}_0^1(Y) + \cdots, \tag{4.5a}$$

$$\hat{\Phi}_0(Y;\,\varepsilon) \;= \hat{\Phi}_0^0(Y) + \underbrace{\varepsilon^{1/2}\hat{\Phi}_0^{1/2}(Y)} + \varepsilon\hat{\Phi}_0^1(Y) + \cdots, \tag{4.5b}$$

where the eigensolution at $O(\varepsilon^{1/2})$, identified with an underbrace, will be required for matching with the solution at the top wall.

At leading order and $O(\varepsilon^{1/2})$,

$$0 = \frac{\mathrm{d}^2\hat{\Phi}_0^j}{\mathrm{d}Y^2}, \tag{4.6a}$$

$$Y\hat{\Phi}_0^j = 2\mathrm{i}\hat{\psi}_0^j. \tag{4.6b}$$

https://doi.org/10.1017/jfm.2016.455 Published online by Cambridge University Press

The dominant balance implies that the polymer torque, $\hat{\chi}_0 \propto -\mathrm{d}_Y^2\hat{\Phi}_0$, is zero to leading order. Equation (4.6*b*) indicates that forces are generated through the action of the base-state streamwise stress on curvature in the perturbation streamlines as the polymer is advected. After applying the boundary conditions at $Y=0$ we find

$$\hat{\psi}_0^0(Y) = Y(A_0 Y - \hat{h}), \quad \hat{\psi}_0^{1/2}(Y) = A_{1/2}Y^2, \tag{4.7a,b}$$

where A_0 and $A_{1/2}$ are constants and $\hat{h} \equiv h/\alpha$. The first-order correction accounts for polymer relaxation and also the influence of the base-state shear stress, T_{12},

$$0 = \frac{\mathrm{d}^2\hat{\Phi}_0^1}{\mathrm{d}Y^2}, \tag{4.8a}$$

$$Y\hat{\Phi}_0^1 - \mathrm{i}\hat{\Phi}_0^0 = 2\mathrm{i}\hat{\psi}_0^1 - 2\frac{\mathrm{d}\hat{\psi}_0^0}{\mathrm{d}Y}. \tag{4.8b}$$

Applying homogeneous boundary conditions at $Y=0$, the streamfunction is $\hat{\psi}_0^1(Y) = A_1Y^2$, and the solution correct to $O(\varepsilon)$ reads

$$\hat{\psi}_0(Y) = Y(A_0Y - \hat{h}) + \varepsilon^{1/2}A_{1/2}Y^2 + \varepsilon A_1 Y^2 + \cdots. \tag{4.9}$$

This expression, which is dictated by elastic effects only, corresponds to a vorticity perturbation which is constant across the channel, $\omega_0(Y) = -2A_0 - 2\varepsilon^{1/2}A_{1/2} - \cdots$. In fact, the elastic flow response (4.9) is a simple distortion of the mean-flow streamlines to mimic the topography of the lower wall across the depth of the channel. As such, it cannot satisfy both boundary conditions at the upper wall, $Y=1$.

Upper wall layer: in order to focus on the upper wall region, we introduce the new coordinate $\eta \equiv (Y-1)/\delta(\varepsilon)$. In terms of η, the bulk streamfunction (4.9) takes the form

$$\hat{\psi}_0(\eta) = A_0 - \hat{h} + \varepsilon^{1/2}[(2A_0 - \hat{h})\eta + A_{1/2}] + \varepsilon(A_0\eta^2 + 2A_{1/2}\eta + A_1) + \cdots. \tag{4.10}$$

Enforcing the no penetration condition at $Y=1$, or $\eta=0$, implies $A_0 = \hat{h}$. There is a non-zero gradient in the streamfunction, or a slip velocity, which must be corrected by the inner solution.

In the wall layer, we define the vorticity and polymer potential, $\{\overline{\psi}_0(\eta), \overline{\Phi}_0(\eta)\} = \{\hat{\psi}_0(Y), \hat{\Phi}_0(Y)\}$, and the rescaled equations (4.2) become,

$$0 = \varepsilon\beta\frac{\mathrm{d}^4\overline{\psi}_0}{\mathrm{d}\eta^4} + \delta^2(1-\beta)\frac{\mathrm{d}^2\overline{\Phi}_0}{\mathrm{d}\eta^2}, \tag{4.11a}$$

$$(1 + \delta\eta - \mathrm{i}\varepsilon)\overline{\Phi}_0 = \left(2\mathrm{i} + 2\frac{\varepsilon}{\delta}\frac{\mathrm{d}}{\mathrm{d}\eta} - \frac{\mathrm{i}\varepsilon^2}{\delta^2}\frac{\mathrm{d}^2}{\mathrm{d}\eta^2}\right)\overline{\psi}_0. \tag{4.11b}$$

Balancing vorticity diffusion in the solvent with polymer torque implies that $\delta = \varepsilon^{1/2}$, which motivates the asymptotic expansion,

$$\overline{\psi}_0(\eta;\varepsilon) = \varepsilon^{1/2}(\overline{\psi}_0^0(\eta) + \varepsilon^{1/2}\overline{\psi}_0^1(\eta) + \cdots), \tag{4.12a}$$

$$\overline{\Phi}_0(\eta;\varepsilon) = \varepsilon^{1/2}(\overline{\Phi}_0^0(\eta) + \varepsilon^{1/2}\overline{\Phi}_0^1(\eta) + \cdots). \tag{4.12b}$$

https://doi.org/10.1017/jfm.2016.455 Published online by Cambridge University Press

At leading order

$$0 = \beta \frac{\mathrm{d}^4 \overline{\psi}_0^0}{\mathrm{d}\eta^4} + (1-\beta)\frac{\mathrm{d}^2 \overline{\Phi}_0^0}{\mathrm{d}\eta^2}, \tag{4.13a}$$

$$\overline{\Phi}_0^0 = 2\mathrm{i}\overline{\psi}_0^0. \tag{4.13b}$$

After eliminating an unphysical solution which grows exponentially as $\eta \to -\infty$ and applying the homogeneous boundary conditions at $\eta = 0$, the leading-order streamfunction is

$$\overline{\psi}_0^0(\eta) = \overline{B}_0(\kappa\eta + 1 - \mathrm{e}^{\kappa\eta}), \tag{4.14}$$

where $\kappa = (1-\mathrm{i})\sqrt{(1-\beta)/\beta}$. At first order there are correction terms due to advection of the polymer and the base shear stress T_{12},

$$0 = \beta \frac{\mathrm{d}^4 \overline{\psi}_0^1}{\mathrm{d}\eta^4} + (1-\beta)\frac{\mathrm{d}^2 \overline{\Phi}_0^1}{\mathrm{d}\eta^2}, \tag{4.15a}$$

$$\overline{\Phi}_0^1 + \eta\overline{\Phi}_0^0 = 2\mathrm{i}\overline{\psi}_0^1 + 2\frac{\mathrm{d}\overline{\psi}_0^0}{\mathrm{d}\eta}. \tag{4.15b}$$

Combining these equations and solving for $\overline{\psi}_0^1$, the inner streamfunction to $O(\varepsilon)$ is

$$\begin{aligned}\overline{\psi}_0(\eta) \;=\; & \varepsilon^{1/2}\overline{B}_0(\kappa\eta + 1 - \mathrm{e}^{\kappa\eta}) \\ & + \varepsilon\left[\overline{B}_1(\kappa\eta + 1 - \mathrm{e}^{\kappa\eta}) + \overline{B}_0\left(\kappa\eta^2 - \frac{(2\mathrm{i}\kappa^2 - 1)\eta}{4} + \frac{\eta}{4}(\kappa\eta - 1 + 2\mathrm{i}\kappa^2)\mathrm{e}^{\kappa\eta}\right)\right].\end{aligned} \tag{4.16}$$

Matching with the inner limit of the streamfunction in the bulk (4.10) determines the unknown constants in both regions,

$$\overline{B}_0 = A_{1/2} = \frac{\hat{h}}{\kappa}, \quad \overline{B}_1 = A_1 = \frac{\hat{h}}{\kappa^2}\left(\frac{7 + 2\mathrm{i}\kappa^2}{4}\right). \tag{4.17a,b}$$

A composite solution is formed by combining the bulk (4.9) and inner (4.16) contributions and subtracting their overlap. It compares favourably to the solution to the long-wave equations (4.3) and also to the full numerical solution of (4.1) in figure 7. In particular, the matched asymptotics are able to accurately capture the amplification of the vorticity near the upper wall.

The asymptotic solution is instructive. Unlike the Hankel function solution of the long-wave equations (4.3), the matched asymptotic solution (4.9), (4.16) delineates the origin of the vorticity distribution across the channel and of the vorticity amplification at the top wall. It also demonstrates that the flow response in the shallow-elastic regime is dominated by elastic effects. The distortion of the highly tensioned mean-flow streamlines by the surface undulations establishes an irrotational polymer force field in the bulk of the channel ($\hat{\chi} \propto -d_Y^2\hat{\Phi} = 0$ in 4.6*a*), which corresponds to a constant perturbation vorticity ($\hat{\omega}_0 \approx -2\hat{h}$ from 4.9). The perturbed, total velocity streamlines are parallel to the bottom wall topography in this layer. Close to the upper wall, the no-slip condition generates large vorticity gradients, with

https://doi.org/10.1017/jfm.2016.455 Published online by Cambridge University Press

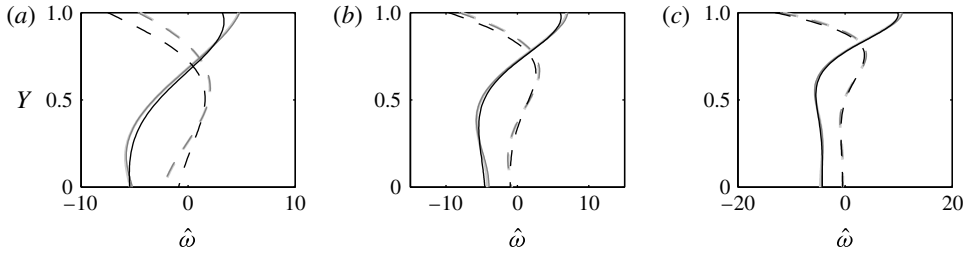


FIGURE 7. Comparison of numerics (grey line), long-wave (dark grey line) and $\mathcal{W} \gg 1$ (black line) solutions for the vorticity, $\hat{\omega} = -\mathrm{d}_Y^2\hat{\psi}$. The parameters correspond to those in figure 6 and from (*a*)–(*c*) $\mathcal{W} = \{10, 20, 40\}$.

corresponding variations in polymer torque. The wall vorticity can be evaluated from the inner solution,

$$\begin{aligned}\hat{\omega}_0(1) &= \frac{\kappa\hat{h}}{\varepsilon^{1/2}} + O(1),\\ &= \kappa\mathcal{W}^{1/2}\hat{h} + O(1),\end{aligned} \tag{4.18}$$

and has been amplified relative to its value in the bulk, $\hat{\omega} \approx -2\hat{h}$, by a factor $\kappa\mathcal{W}^{1/2}$. This effect is therefore increasingly important with increasing polymer concentration and elasticity

4.2. *Deep-elastic flow*

The terminology 'deep elastic' refers to flow configurations where $\alpha \gtrsim 1$ and $\Sigma \gtrsim 1$. The second of these requirements places the critical layer sufficiently far from the wall such that vorticity wave propagation dominates the dynamics of the perturbation field rather than base-flow advection. Two examples of the vorticity induced by the lower wall in this regime are reported in figure 8, alongside a Newtonian solution from the deep-viscous regime. The vorticity appears unchanged from the Newtonian solution irrespective of the choice of parameters, and $|\hat{\omega}|$ is monotonically decaying with height.

In this section we construct an asymptotic solution to (2.7) assuming $\Sigma \gg 1$, and demonstrate that the vorticity is unchanged from the Newtonian deep-viscous solution for any choice of W or β. We then examine the high-Weissenberg-number limit in order to explain why the polymer does not alter the structure of the perturbation field in deep channels with high elasticity.

We assume that $\alpha \gg 1$ so that the upper wall no longer appears in the problem. Then, defining the scaled polymer potential $\Phi \equiv \varphi/W$, the governing system (2.7) becomes

$$\mathrm{i}k\dot{\gamma}y\left(\frac{\mathrm{d}^2}{\mathrm{d}y^2} - k^2\right)\psi = \frac{\Sigma^2}{2}\left[\frac{\beta}{(1-\beta)W}\left(\frac{\mathrm{d}^2}{\mathrm{d}y^2} - k^2\right)^2\psi + \left(\frac{\mathrm{d}^2}{\mathrm{d}y^2} - k^2\right)\Phi\right], \tag{4.19a}$$

$$\left(\mathrm{i}k\dot{\gamma}y + \frac{1}{W}\right)\Phi = \left[-2k^2\dot{\gamma}^2 + \frac{2\mathrm{i}\dot{\gamma}}{W}\frac{\mathrm{d}}{\mathrm{d}y} + \frac{1}{W^2}\left(\frac{\mathrm{d}^2}{\mathrm{d}y^2} - k^2\right)\right]\psi. \tag{4.19b}$$

https://doi.org/10.1017/jfm.2016.455 Published online by Cambridge University Press

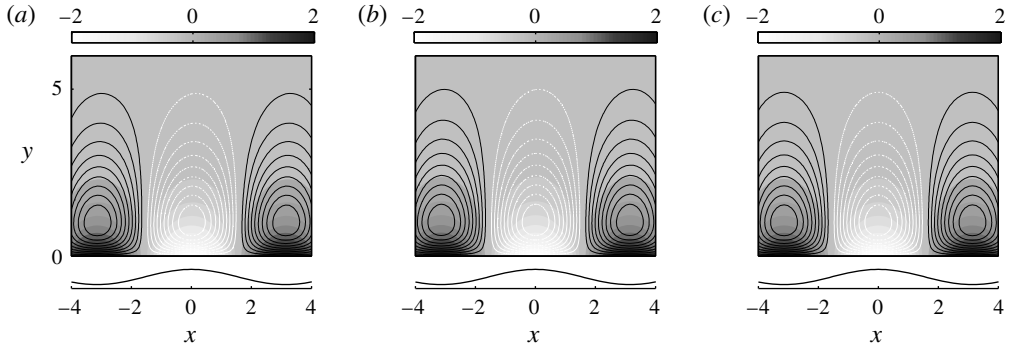


FIGURE 8. Vortical perturbations (top) induced by the wavy wall (bottom) in the deep-elastic regime. Filled contours are the spanwise vorticity, lines are the streamfunction. (*a*) Newtonian flow (deep viscous) $\alpha = 10$, $R = 5$. (*b*) Deep-elastic flow, $\alpha = 10$ and $\Sigma = 8.9$ with $R = 5$, $\beta = 0.8$, $W = 10$. (*c*) Deep-elastic flow, $\alpha = 10$ and $\Sigma = 34.6$ with $R = 5$, $\beta = 0.5$, $W = 60$.

Assuming that the critical layer is far above the lower wall $\Sigma \gg 1$, we seek a solution in powers of $\varepsilon \equiv 1/\Sigma^2 \ll 1$,

$$\psi(y;\,\varepsilon) = \psi_0(y) + \varepsilon\psi_1(y) + \cdots, \tag{4.20a}$$

$$\Phi(y;\,\varepsilon) = \Phi_0(y) + \varepsilon\Phi_1(y) + \cdots, \tag{4.20b}$$

At leading order only the advection term in the Orr–Sommerfeld equation vanishes, leaving the inertialess system

$$0 = \frac{\beta}{W}\left(\frac{\mathrm{d}^2}{\mathrm{d}y^2} - k^2\right)^2 \psi_0 + (1-\beta)\left(\frac{\mathrm{d}^2}{\mathrm{d}y^2} - k^2\right)\Phi_0, \tag{4.21a}$$

$$\left(\mathrm{i}k\dot{\gamma}y + \frac{1}{W}\right)\Phi_0 = \left[-2k^2\dot{\gamma}^2 + \frac{2\mathrm{i}\dot{\gamma}}{W}\frac{\mathrm{d}}{\mathrm{d}y} + \frac{1}{W^2}\left(\frac{\mathrm{d}^2}{\mathrm{d}y^2} - k^2\right)\right]\psi_0. \tag{4.21b}$$

Note that we have not yet invoked any assumptions regarding the magnitude of the Weissenberg number. These equations may be combined and written in the form of an inhomogeneous confluent hypergeometric equation, and the leading-order streamfunction is

$$\begin{aligned}\psi_0(y) \;=\; & E_0 y\mathrm{e}^{-ky} + F_0 y\mathrm{e}^{ky} \\ & + G_0\mathrm{e}^{-ky}\mathcal{U}\left(\frac{(1-\beta)(1-\mathrm{i}\dot{\gamma}W)}{\beta}, \frac{2(1-\beta)}{\beta}, 2\left(ky + \frac{1}{\mathrm{i}\dot{\gamma}W\beta}\right)\right) \\ & + H_0\mathrm{e}^{-ky}\mathcal{M}\left(\frac{(1-\beta)(1-\mathrm{i}\dot{\gamma}W)}{\beta}, \frac{2(1-\beta)}{\beta}, 2\left(ky + \frac{1}{\mathrm{i}\dot{\gamma}W\beta}\right)\right),\end{aligned} \tag{4.22}$$

where $\mathcal{U}$ and $\mathcal{M}$ are Kummer's functions (Abramowitz & Stegun 1964). After discarding exponentially growing terms and applying the boundary conditions at the lower wall, we obtain $\psi_0(y) = -h\dot{\gamma}y\mathrm{e}^{-ky}$, which is identical to the leading-order Newtonian solution in the deep-viscous regime reported by Charru & Hinch (2000). The polymer does not have an effect on the flow field to leading order for any value of W provided $\Sigma \gg 1$.

https://doi.org/10.1017/jfm.2016.455 Published online by Cambridge University Press

The above result is simple to understand in the limit of fast polymer relaxation, $W \ll 1$. As noted in § 3.1, in this limit the polymer behaves like additional solvent, $\Phi_0 \sim (1/2W)(\mathrm{d}_y^2 - k^2)\psi_0$. The flow is therefore dominated by vorticity diffusion, and the streamfunction satisfies the biharmonic equation $(\mathrm{d}_y^2 - k^2)^2\psi_0 = 0$.

Some additional explanation is required in the high-Weissenberg-number limit, where it is not obvious why the flow response should appear unaffected by the large base-state stress. If $W \gg 1$, we may approximate (4.21) by

$$0 = \left(\frac{\mathrm{d}^2}{\mathrm{d}y^2} - k^2\right)\Phi_0 = -X_0, \tag{4.23a}$$

$$\mathrm{i}k\dot{\gamma}y\Phi_0 = -2k^2\dot{\gamma}^2\psi_0, \tag{4.23b}$$

where $X_0 = \chi_0/W$ is the scaled polymer torque. The dominant balance is analogous to the large-$\mathcal{W}$ limit of the long-wave equations (4.6). According to (4.23*b*), polymer forces are generated by displacement of the highly tensioned mean-flow streamlines, similar to the flow in the shallow-elastic regime. However, without the influence of the upper wall, there is no reason for a rapid flow adjustment and the Orr–Sommerfeld equation (4.23*a*) indicates that the irrotational polymer force field decays exponentially in y. This results in a perturbation flow which has the same form as the Newtonian deep-viscous regime.

4.3. *Transcritical flow*

The terminology 'transcritical' is associated with flows where $\alpha > \Sigma$ and $\Sigma \lesssim 1$. These criteria correspond to the existence of a critical layer inside the flow domain and whose height, $y = \Sigma$ or $y^* = \sqrt{2\nu_p\varsigma}$, is within one wavelength from the lower wall. Across this critical layer, the base-flow velocity changes from subcritical to supercritical relative to the vorticity longitudinal wave speed. It is the same surface across which Yoo & Joseph (1985) find a change in type in the equations for an upper convected Maxwell fluid. Here, the focus is the mechanism for vorticity amplification at this layer.

The spanwise-vorticity perturbation and associated streamfunction that are induced by the wavy wall are reported in figure 9 for three transcritical conditions. The critical layer height, Σ, is held constant, and the bulk Reynolds and Weissenberg numbers are varied. In each case the spanwise vorticity is amplified around $y = \Sigma$. The ω-perturbation field close to $y = \Sigma$ is arranged in stripes of positive and negative vorticity which are tilted forward with the shear and which become progressively stronger as R and W are increased.

In figure 10, α is varied while the bulk flow parameters are held fixed, which corresponds to a fixed vorticity wave speed. As a result, the dimensional y^*-location of the critical layer is unchanged. However, relative to the roughness length scale, the critical layer height, $y = \Sigma$, increases with α and figure 10 captures the transition between the transcritical and deep-elastic regimes. As Σ increases, the vorticity decays with height in $y \lesssim \Sigma$ and amplification at $y = \Sigma$ is much less effective.

In order to examine the vorticity generation at the critical layer, the high-Weissenberg-number limit of the governing equations (2.7) will be derived. In this limit only the effects of the kinematic torque amplification mechanism and streamwise normal stress remain in the polymer-torque equation. The kinematic amplification is interpreted in terms of the polymer forces, before the equations for ω and χ are combined to form an 'elastic-Rayleigh' equation for the spanwise vorticity. In this

https://doi.org/10.1017/jfm.2016.455 Published online by Cambridge University Press

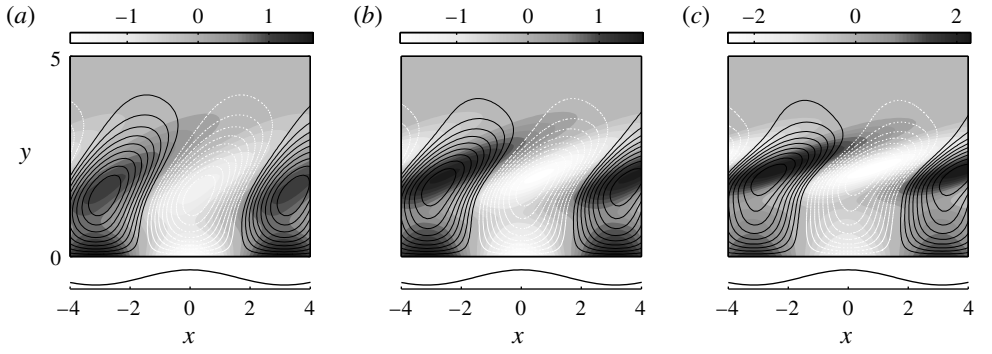


FIGURE 9. Vortical perturbations (top) induced by the wavy wall (bottom) in transcritical flows with constant $\alpha = 10$ and $\Sigma = 2.45$. Filled contours are the spanwise vorticity, lines are the streamfunction. The polymer viscosity is fixed at $\beta = 0.5$ and the bulk Reynolds and Weissenberg numbers are varied: (*a*) $R = 250$, $W = 15$; (*b*) $R = 500$, $W = 30$; (*c*) $R = 1000$, $W = 60$.

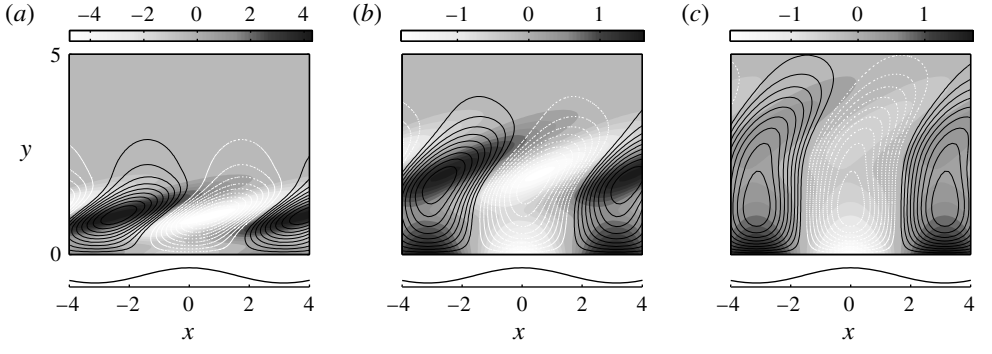


FIGURE 10. Vortical perturbations (top) induced by the wavy wall (bottom) in transcritical flows with constant vorticity wave speed, $\sqrt{2W(1-\beta)/R} = 0.24$ ($R = 500$, $W = 30$, $\beta = 0.5$), with varying α. Filled contours are the spanwise vorticity, lines are the streamfunction. (*a*) $\alpha = 5$; (*b*) $\alpha = 10$; (*c*) $\alpha = 15$.

equation the torque kinematics appear as a forcing term, and the efficacy of this term to generate vorticity is shown to depend on the relative values of two frequencies: the frequency at which the lower wall appears to oscillate relative to an observer moving with the shear and the frequency of a streamwise-travelling elastic vorticity wave with wavenumber k. We demonstrate that there is a resonance between these two frequencies at the critical layer, before developing an approximate solution for the perturbation streamfunction using matched asymptotic expansions. The solution provides explicit expressions for the critical layer thickness and the level of vorticity amplification due to the resonance at $y = \Sigma$.

The vorticity amplification in the transcritical regime is increasingly pronounced at large Weissenberg numbers. Therefore, the small parameter, $\varepsilon \equiv 1/W \ll 1$, is defined and an asymptotic expansion is adopted,

$$\psi(y;\varepsilon) = \psi_0(y) + \varepsilon\psi_1(y) + \cdots, \tag{4.24a}$$

$$\Phi(y;\varepsilon) = \Phi_0(y) + \varepsilon\Phi_1(y) + \cdots, \tag{4.24b}$$

https://doi.org/10.1017/jfm.2016.455 Published online by Cambridge University Press

where $\Phi = \varepsilon\varphi$ is the scaled polymer potential. The leading-order approximation of (2.7) is

$$\mathrm{i}k\dot{\gamma}y\left(\frac{\mathrm{d}^2}{\mathrm{d}y^2} - k^2\right)\psi_0 = \frac{\Sigma^2}{2}\left(\frac{\mathrm{d}^2}{\mathrm{d}y^2} - k^2\right)\Phi_0, \tag{4.25a}$$

and

$$\mathrm{i}k\dot{\gamma}y\Phi_0 = -2k^2\dot{\gamma}^2\psi_0. \tag{4.25b}$$

Again, the high-Weissenberg-number limit means that polymer forces are primarily generated by an induced curvature in the tensioned mean-flow streamlines. In this particular regime, it is instructive to write (4.25) in terms of the vorticity, ω, and polymer torque, χ (cf. equation (2.9)),

$$\mathrm{i}k\dot{\gamma}y\omega_0 = \frac{\Sigma^2}{2}X_0, \tag{4.26a}$$

$$\mathrm{i}k\dot{\gamma}yX_0 = \underbrace{2\mathrm{i}k\dot{\gamma}\frac{\mathrm{d}\Phi_0}{\mathrm{d}y}}_{\mathscr{S}} - 2k^2\dot{\gamma}^2\omega_0, \tag{4.26b}$$

where $X \equiv \varepsilon\chi = -(\mathrm{d}_y^2 - k^2)\Phi$. The term labelled $\mathscr{S}$ corresponds to the kinematic mechanism for polymer-torque amplification,

$$\mathscr{S} \equiv 2\mathrm{i}k\dot{\gamma}\frac{\mathrm{d}\Phi_0}{\mathrm{d}y} = \dot{\gamma}\left(\mathrm{i}k\tilde{f}_x - \frac{\mathrm{d}\tilde{f}_y}{\mathrm{d}y}\right), \tag{4.27}$$

and $\tilde{f}_i \equiv \varepsilon f_i$ are the scaled polymer forces. The relative realignment of streamwise layers of varying polymer force by the mean shear generates a perturbation torque at a point.

Combining (4.26) into a single equation yields

$$(\varpi^2(y) - k^2c_\omega^2)\omega_0 = -\mathrm{i}kc_\omega\Sigma\frac{\mathrm{d}\Phi_0}{\mathrm{d}y}, \tag{4.28}$$

where $\varpi(y) \equiv k\dot{\gamma}y$ is the apparent frequency at which the vorticity source (lower wall) appears to oscillate relative to an observer travelling with the mean flow at a height y, while $c_\omega \equiv \dot{\gamma}\Sigma$ is the dimensionless speed of a streamwise-travelling vorticity wave in the viscoelastic flow. The kinematic torque amplification appears as a forcing term on the right-hand side. Equation (4.28) is known as the elastic-Rayleigh equation (Azaiez & Homsy 1994; Rallison & Hinch 1995; Ray & Zaki 2014, 2015).

In equation (4.28), kc_ω represents the frequency of an elastic vorticity with wavenumber k and appears as the natural frequency. At the critical layer, $y = \Sigma$, a travelling observer sees the wall as a vorticity source sweeping by at the elastic wave speed. Or, equivalently, the critical layer is the height where a travelling observer sees perturbations oscillating with a frequency that matches the frequency of an elastic wave of the same wavelength. The resulting resonance at the particular location in the flow corresponds to a singular point in the elastic-Rayleigh equation, and the torque amplification mechanism becomes most effective.

While equation (4.28) identifies the mechanism for vorticity amplification around $y = \Sigma$, the thickness of the critical layer is unknown. Furthermore, the level of vorticity amplification at the critical layer cannot be deduced from (4.28), in

https://doi.org/10.1017/jfm.2016.455 Published online by Cambridge University Press

which $y = \Sigma$ is a singular point. In order to address these issues, a solution to the viscoelastic Orr–Sommerfeld system (2.7) is now constructed using matched asymptotic expansions with $\varepsilon \equiv 1/W \ll 1$ as the small parameter.

Bulk solution: the leading term in an expansion in powers of ε satisfies the elastic-Rayleigh equation derived above (4.28), which determines the perturbation field in the bulk of the channel. In terms of the streamfunction, ψ_0, this equation is,

$$\frac{\mathrm{d}^2}{\mathrm{d}y^2}\left(\frac{\psi_0}{y}\right) + \frac{2y}{(y^2-\Sigma^2)}\frac{\mathrm{d}}{\mathrm{d}y}\left(\frac{\psi_0}{y}\right) - k^2\left(\frac{\psi_0}{y}\right) = 0. \tag{4.29}$$

Equation (4.29) has regular singular points at $y = \Sigma$ and $y = -\Sigma$, the second of which lies outside of the flow domain. The solution may therefore be sought as a Frobenius series around $y = \Sigma$ (Bender & Orszag 1978). Above the critical layer, $y > \Sigma$, the expression for $\psi_0(y)$ is

$$\psi_0^+(y) = A_0^+ y\sum_{j=0}^{\infty} b_j\,(y-\Sigma)^j + B_0^+ y\left(\sum_{j=1}^{\infty} c_j\,(y-\Sigma)^j + \sum_{j=0}^{\infty} b_j (y-\Sigma)^j \log|y-\Sigma|\right). \tag{4.30a}$$

The series coefficients, b_j and c_j, are provided in appendix A. Below the critical layer the streamfunction is written

$$\psi_0^-(y) = A_0^- y\sum_{j=0}^{\infty} b_j (y-\Sigma)^j + B_0^- y\left(\sum_{j=1}^{\infty} c_j (y-\Sigma)^j + \sum_{j=0}^{\infty} b_j (y-\Sigma)^j (\log|y-\Sigma| - \mathrm{i}\pi)\right), \tag{4.30b}$$

where the branch chosen for the logarithm is not arbitrary, but is motivated by the solution in the critical layer which is constructed below. Note that the series (4.30) have a radius of convergence which extends only as far as the next singular point of the elastic-Rayleigh equation (4.29), which is at $y = -\Sigma$. Therefore, the expression for $\psi_0^+(y)$ (4.30*a*) only converges below $y = 3\Sigma$. However, the present focus is the behaviour around the critical layer, $y = \Sigma$, and we do not attempt to patch this series to an expression valid for large y.

Critical layer: the kinematic amplification mechanism is most effective at the critical layer. At this location a resonance occurs between the oscillation frequency of the wall vorticity, as measured by an observer travelling with the base flow, and the frequency of an elastic wave with wavenumber k. This behaviour corresponds to a singular point in the elastic-Rayleigh equation (4.29) and motivates an examination of the Orr–Sommerfeld system (2.7) in the vicinity of the critical layer. We assume an internal boundary layer at $y = \Sigma$ of thickness $\delta_c(\varepsilon)$ and adopt the rescaling $\eta \equiv (y-\Sigma)/\delta_c(\varepsilon)$. In terms of η the bulk Frobenius solutions (4.30),

$$\psi_0^+(\eta) \sim A_0^+\Sigma + B_0^+\Sigma(\log|\eta| + \log\delta_c) + \cdots, \tag{4.31a}$$

$$\psi_0^-(\eta) \sim A_0^-\Sigma + B_0^-\Sigma(\log|\eta| - \mathrm{i}\pi + \log\delta_c) + \cdots, \tag{4.31b}$$

which suggests an inner expansion of the form

$$\overline{\psi}(\eta) = \log\delta_c\,\overline{\psi}_{-1}(\eta) + \overline{\psi}_0(\eta) + \cdots, \tag{4.32}$$

where $\overline{\psi}(\eta) = \psi(y)$ is the streamfunction expressed in terms of the critical layer coordinate and the term appearing at $O(\log\,\delta_c)$ is an eigensolution required for matching.

https://doi.org/10.1017/jfm.2016.455 Published online by Cambridge University Press

In terms of the stretched coordinate, η, the full Orr–Sommerfeld system (2.7) becomes,

$$\mathrm{i}k\dot{\gamma}(\Sigma+\delta_c\eta)\left(\frac{1}{\delta_c^2}\frac{\mathrm{d}^2}{\mathrm{d}\eta^2}-k^2\right)\overline{\psi}=\frac{\Sigma^2}{2}\left[\frac{\beta\varepsilon}{(1-\beta)}\left(\frac{1}{\delta_c^2}\frac{\mathrm{d}^2}{\mathrm{d}\eta^2}-k^2\right)^2\overline{\psi}+\left(\frac{1}{\delta_c^2}\frac{\mathrm{d}^2}{\mathrm{d}\eta^2}-k^2\right)\overline{\Phi}\right], \tag{4.33a}$$

$$\mathrm{i}k\dot{\gamma}(\Sigma+\delta_c\eta)\overline{\Phi}+\varepsilon\overline{\Phi}=\left[-2k^2\dot{\gamma}^2+2\mathrm{i}k\dot{\gamma}\frac{\varepsilon}{\delta_c}\frac{\mathrm{d}}{\mathrm{d}\eta}+\varepsilon^2\left(\frac{1}{\delta_c^2}\frac{\mathrm{d}^2}{\mathrm{d}\eta^2}-k^2\right)\right]\overline{\psi}, \tag{4.33b}$$

where $\overline{\Phi}(\eta)=\Phi(y)$ is the scaled polymer potential. If $\delta_c>\varepsilon$, then according to (4.33*b*) the polymer potential $\overline{\Phi}$ is dominated by the effects of the normal stress, T_{11}, similar to the bulk flow (4.30). This balance implies that $\mathrm{i}k\dot{\gamma}(\Sigma+\delta_c\eta)\overline{\Phi}\approx-2k^2\dot{\gamma}^2\overline{\psi}$, which is substituted into (4.33*a*) and yields,

$$\begin{aligned}&\mathrm{i}k\dot{\gamma}(\Sigma+\delta_c\eta)\left(\frac{1}{\delta_c^2}\frac{\mathrm{d}^2}{\mathrm{d}\eta^2}-k^2\right)\overline{\psi}\\&\quad\approx\frac{\Sigma^2}{2}\left[\frac{\beta\varepsilon}{(1-\beta)}\left(\frac{1}{\delta_c^2}\frac{\mathrm{d}^2}{\mathrm{d}\eta^2}-k^2\right)^2\overline{\psi}+\underbrace{\frac{2\mathrm{i}k\dot{\gamma}}{\Sigma}\left(\frac{1}{\delta_c^2}\frac{\mathrm{d}^2}{\mathrm{d}\eta^2}-k^2\right)\left(\overline{\psi}-\frac{\delta_c\eta}{\Sigma}\overline{\psi}+\cdots\right)}_{\overline{\Phi}}\right],\end{aligned} \tag{4.34}$$

As anticipated, the leading term in $\overline{\Phi}$ on the right-hand side cancels with the leading advection term on the left-hand side. The dominant balance between advection, diffusion in the solvent and polymer potential due to T_{11} then suggests a critical layer thickness

$$\delta_c=\left(\frac{\varepsilon\beta\Sigma^2}{4\dot{\gamma}k(1-\beta)}\right)^{1/3}, \tag{4.35}$$

where the factor of 4 is introduced for convenience. In dimensional variables $\delta_c^*=(\nu_s/2\dot{\gamma}^*k^*)^{1/3}$, which is a diffusion length in the solvent. The scaling is also consistent with the original assumption regarding the relative importance of the base-state stresses in the critical layer: T_{12} appears at $O(\varepsilon^{2/3})$ in (4.33*b*).

The dominant balance between advection, polymer torque generated by T_{11} and solvent diffusion in (4.34) leads to

$$\frac{\mathrm{d}^4\overline{\psi}_i}{\mathrm{d}\eta^4}-\frac{\mathrm{d}}{\mathrm{d}\eta}\left(\mathrm{i}\eta\frac{\mathrm{d}\overline{\psi}_i}{\mathrm{d}\eta}\right)=0, \tag{4.36}$$

which is satisfied by the two leading terms in the inner expansion (4.32). Equation (4.36) can be written as an inhomogeneous Airy equation for the derivative $\mathrm{d}_\eta\overline{\psi}_0$, although it is more convenient to express the solutions in integral form,

$$\begin{aligned}\overline{\psi}_i(\eta)\;=\;&\overline{A}_i+\overline{B}_i\int_\sigma^\infty\left(\frac{1}{s}\right)\exp\left(-\frac{s^3}{3}-\mathrm{i}s\eta\right)\mathrm{d}s\\&+\overline{C}_i\int_\sigma^\infty\left(\frac{1}{s}\right)\exp\left(-\frac{s^3}{3}+\frac{s\eta(\sqrt{3}+\mathrm{i})}{2}\right)\mathrm{d}s\\&+\overline{D}_i\int_\sigma^\infty\left(\frac{1}{s}\right)\exp\left(-\frac{s^3}{3}+\frac{s\eta(-\sqrt{3}+\mathrm{i})}{2}\right)\mathrm{d}s,\end{aligned} \tag{4.37}$$

https://doi.org/10.1017/jfm.2016.455 Published online by Cambridge University Press

where the limit $\sigma \to 0$ should be taken and the constant $\overline{A}_i$ contains terms which eliminate the logarithmic divergence associated with this limit (see appendix A). This statement is made explicit below, where $\overline{\psi}(\eta)$ is matched to the elastic-Rayleigh solutions in the bulk.

Assuming that the critical layer and the wall are well separated, $\Sigma \gg \delta_c$, solutions which are exponentially growing as $\eta \to \pm\infty$ must be discarded. The critical layer streamfunction thus takes the form,

$$\overline{\psi}_i(\eta) = \overline{A}_i + \overline{B}_i \int_\sigma^\infty \left(\frac{1}{s}\right) \exp\left(-\frac{s^3}{3} - \mathrm{i}s\eta\right) \mathrm{d}s. \tag{4.38}$$

In appendix A the method of steepest descents is applied to the integral appearing in (4.38) to obtain the behaviour of the inner streamfunction as $\eta \to \pm\infty$,

$$\overline{\psi}_i(\eta \to \infty) \sim \overline{A}_i + \overline{B}_i \left(-\gamma - \frac{\mathrm{i}\pi}{2} - \log\sigma - \log|\eta|\right), \tag{4.39a}$$

$$\overline{\psi}_i(\eta \to -\infty) \sim \overline{A}_i + \overline{B}_i \left(-\gamma + \frac{\mathrm{i}\pi}{2} - \log\sigma - \log|\eta|\right), \tag{4.39b}$$

where $\gamma = 0.5772\ldots$ is the Euler–Mascheroni constant and there is a phase change of π across the critical layer. Matching these expressions to the bulk streamfunction near $y = \Sigma$ (4.31) reduces the number of unknown constants in the system to two. Across the critical layer, the constants in the expressions for the bulk streamfunction (4.30) are unchanged,

$$\left.\begin{aligned} A_0^+ = A_0^- \equiv A_0, \\ B_0^+ = B_0^- \equiv B_0. \end{aligned}\right\} \tag{4.40}$$

The constants appearing in the critical layer solution are,

$$\left.\begin{aligned} \overline{A}_{-1} = \Sigma B_0, \quad \overline{B}_{-1} = 0; \\ \overline{A}_0 = \Sigma A_0 + \Sigma B_0 \left(-\gamma - \frac{\mathrm{i}\pi}{2} - \log\sigma\right), \quad \overline{B}_0 = -\Sigma B_0. \end{aligned}\right\} \tag{4.41}$$

The $O(\log\,\delta_c)$ term in the critical layer is therefore a constant, and the inner streamfunction is

$$\overline{\psi}(\eta) = \Sigma B_0 \log\delta_c + \Sigma A_0 + \Sigma B_0\left(-\gamma - \frac{\mathrm{i}\pi}{2} - \log\sigma\right) - \Sigma B_0 \int_\sigma^\infty \left(\frac{1}{s}\right) \exp\left(-\frac{s^3}{3} - \mathrm{i}s\eta\right) \mathrm{d}s. \tag{4.42}$$

In the limit $\sigma \to 0$ the term $-\Sigma B_0 \log\sigma$ eliminates the logarithmic divergence associated with the lower limit of the integral.

The solutions to the elastic-Rayleigh equation (4.30) automatically satisfy the no penetration condition at the lower wall, $\psi_0^-(y = 0) = 0$. One of the two remaining constants, A_0 and B_0, can be eliminated by applying the slip condition on the streamwise perturbation velocity, $\mathrm{d}_y\psi_0^-(y = 0) = -\dot{\gamma}h$. In deep channels, $\alpha \gg 1$, the final constant would be chosen to enforce boundedness of the streamfunction far above the critical layer. In the present formulation, the series solutions to the elastic-Rayleigh equation only converge below $y = 3\Sigma$, and so this condition cannot be enforced without patching $\psi_0^+(y)$ to solutions valid for large y. However, our focus is the vorticity amplification at the critical layer, while above $y \approx \Sigma$ the perturbation decays. Therefore, we instead impose the artificial condition $\psi_0^+(y = 8\Sigma/3) = 0$

https://doi.org/10.1017/jfm.2016.455 Published online by Cambridge University Press

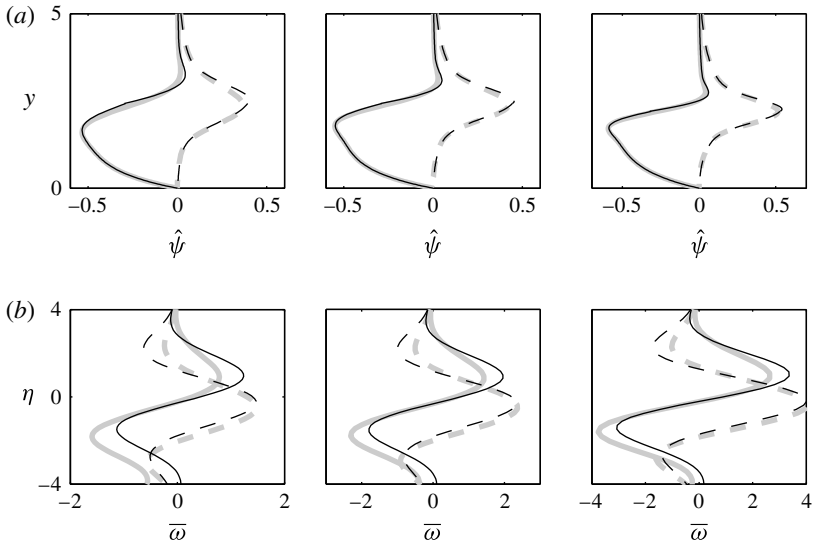


FIGURE 11. Comparison of numerical (grey) and asymptotic (black) solutions in the transcritical regime. (*a*) Composite streamfunction formed from solutions to the elastic-Rayleigh (4.30) and critical layer (4.42) equations. (*b*) Critical layer vorticity, $\overline{\omega}$. From left to right: $\alpha = 10,\ \Sigma = 2.5$, with $R = 500,\ W = 30,\ \beta = 0.5$; $\alpha = 10,\ \Sigma = 2.5$, with $R = 1000,\ W = 60,\ \beta = 0.5$; $\alpha = 10,\ \Sigma = 2.24$, with $R = 2000,\ W = 100,\ \beta = 0.5$.

in order to determine the final unknown constant. In domains where $\alpha < 3\Sigma$, we may enforce the no-penetration condition at the top wall, $\psi_0^+(y = \alpha) = 0$. This approach introduces a small slip velocity, which could be eliminated by examining the perturbations in a thin solvent boundary layer at $y = \alpha$, similar to the approach taken in the shallow-elastic regime (see § 4.1).

A composite asymptotic solution is formed by combining the bulk (4.30) and inner (4.42) solutions and subtracting their overlapping values. It is compared to numerical solutions for three parameter sets in the transcritical regime in figure 11(*a*). The asymptotic solution compares favourably with the numerics, and becomes increasingly accurate as the Weissenberg number is increased.

The critical layer vorticity computed from the inner solution (4.42) is also compared to the numerical solution in figure 11(*b*), with increasingly good agreement at higher W. Furthermore, the vorticity at the critical layer may be estimated explicitly,

$$\begin{aligned}\omega_0(y = \Sigma) &= -\frac{\Sigma B_0}{\delta_c^2}\int_0^\infty s\exp\left(-\frac{s^3}{3}\right)\mathrm{d}s,\\ &= -\frac{\Sigma B_0 3^{-1/3}}{\delta_c^2}\Gamma\left(\frac{2}{3}\right) \approx -\frac{0.9389\,\Sigma B_0}{\delta_c^2}.\end{aligned} \tag{4.43}$$

Numerical calculations of B_0 over a range of Σ (not shown) demonstrate a dependence $B_0 \propto \sqrt{\Sigma}\exp(-\Sigma)$ and so the vorticity $\omega_0 \propto \Sigma^{3/2}\exp(-\Sigma)/\delta_c^2$. The exponential decay with Σ reflects the weakened propensity for vorticity amplification as the critical layer is moved farther from the wall due to decay in $y < \Sigma$, as was remarked in connection with figure 10. The dependence on the solvent diffusion length is intuitive: increasingly sharp gradients are generated across thinner critical layers.

https://doi.org/10.1017/jfm.2016.455 Published online by Cambridge University Press

The transcritical regime, $\alpha > \Sigma$ and $\Sigma \lesssim 1$, is perhaps the most intriguing in the phase diagram because the maximum vorticity is observed in the bulk of the fluid, away from the bottom topography. This non-local vorticity amplification was explained using the elastic-Rayleigh equation which shows that when curvature acts onto the base-state T_{11} stresses, it generates polymer torque. This torque then acts as forcing on the right-hand side of the vorticity equation, and its effectiveness at generating vorticity depends on the difference between two frequencies: (i) the frequency of oscillation of the vorticity source, or the undulating wall, relative to an observer travelling with the mean flow; (ii) the frequency of a streamwise-travelling elastic vorticity wave with wavenumber k, which is a property of the viscoelastic flow configuration. When the two frequencies match, resonance occurs at the critical layer $y = \Sigma$, and the kinematic mechanism becomes most effective at generating vorticity. The critical layer thickness scales with the solvent diffusion, $\delta_c^* \sim (\nu_s/\gamma^* k^*)^{1/3}$ and the vorticity in this layer can be estimated by $\omega = O(\Sigma^{3/2}\exp(-\Sigma)/\delta_c^2)$.

5. Localized roughness

The detailed analysis of the three regimes of vorticity generation above a harmonic wall topography provides the foundation for examining the flow response to general, small-amplitude surface topography. In this section the flow response to localised wall roughness is examined numerically. The phenomenology observed in these computations are then interpreted based on the analyses in § 4.

5.1. *Gaussian wall bump*

By exploiting the linearity of the problem, we herein extend our earlier analyses to more realistic, localized surface topographies using Fourier synthesis. We consider the flow response to a Gaussian wall bump,

$$\mathscr{H}^*(x) = h^* \mathrm{e}^{-|x^*|^2/l_x^{*2}}, \tag{5.1a}$$

where l_x^* is now used as the reference length. The corresponding non-dimensional wall disturbance is $\mathscr{H}'(x) = h\mathrm{e}^{-|x|^2/l_x^2}$, where $l_x = 1$ is retained for clarity. The Fourier transform of this wall bump is also Gaussian

$$\mathscr{H}(k) = \int_{-\infty}^{\infty} \mathscr{H}'(x)\mathrm{e}^{-\mathrm{i}kx}\,\mathrm{d}x = h l_x \sqrt{\pi}\,\mathrm{e}^{-l_x^2 k^2/4}, \tag{5.1b}$$

and we adopt the normalization $h = 1$. Note that the zeroth wavenumber, $k = 0$, corresponds to a mean-flow correction and is omitted from the energy and enstrophy spectra presented in this section.

While the spectral make-up of the wall disturbance (5.1*b*) includes waves for which the channel will appear shallow ($k \to 0$) and infinitely deep ($k \to \infty$), it is helpful to introduce the parameters,

$$\alpha_l \equiv \frac{d}{l_x^*}, \quad \Sigma_l \equiv \frac{\sqrt{2\nu_p \varsigma}}{l_x^*}, \tag{5.2a,b}$$

in order to relate the present results to the earlier discussion of the wavy wall. These parameters are the normalized channel depth and ratio of the critical layer depth to the bump length scale, respectively.

https://doi.org/10.1017/jfm.2016.455 Published online by Cambridge University Press

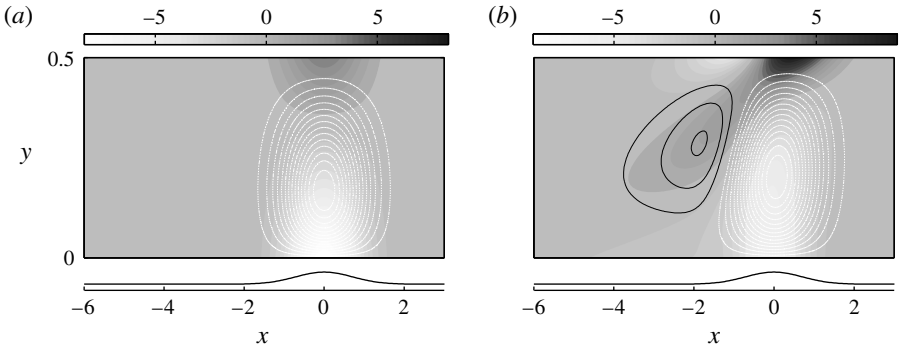


FIGURE 12. Vortical perturbations (top) induced by Gaussian wall bump (bottom) in shallow flow with $\alpha_l = 0.5$. Filled contours are the spanwise vorticity, lines are the streamfunction. (*a*) Newtonian flow with $R = 1$. (*b*) Viscoelastic flow with $\Sigma_l = 3.16$ with $\beta = 0.5,\ W = 40,\ R = 1$.

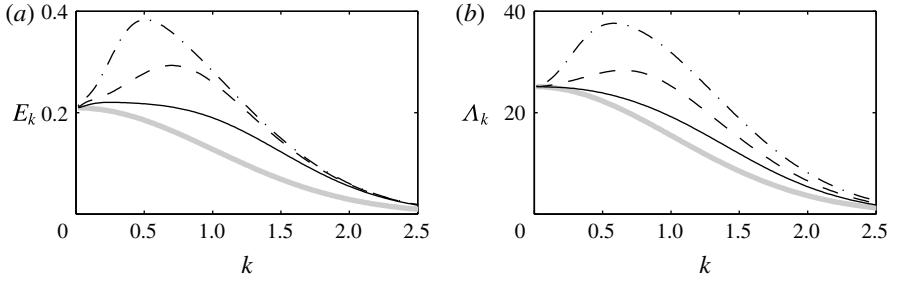


FIGURE 13. Streamwise energy (*a*) and enstrophy (*b*) spectra in a shallow channel with $\alpha_l = 0.5$. Here $R = 1,\ \beta = 0.5$. Grey solid line, Newtonian flow; black solid line, $W = 20$; dashed line, $W = 40$; dot-dashed line, $W = 80$.

The flow response to the Gaussian wall disturbance in a shallow channel, $\alpha_l < 1$, is reported in figure 12 for both Newtonian and Oldroyd-B fluids. Inertial effects are weak, which places the Newtonian flow in the 'shallow-viscous' regime. In the viscoelastic fluid, the high Weissenberg number places the critical layer outside of the flow domain, $\Sigma_l > \alpha_l$, and the flow response can be classified as 'shallow elastic'.

In the Newtonian fluid the Gaussian bump produces an upward distortion of the streamlines, symmetric about the bump centre, $x = 0$. This inertialess behaviour corresponds to a single vortex in the perturbation field directly above the bump. In the viscoelastic fluid the flow response is not symmetric with respect to the bump centre. Instead, a second counter-rotating vortex is formed upstream of the bump. This second vortex is attached to a region of positive spanwise vorticity extending down from the top wall where the vorticity magnitude is maximum.

The response of a viscoelastic fluid to the Gaussian bump in a shallow channel is further examined in figure 13, where streamwise energy and enstrophy spectra are reported for increasing values of the Weissenberg number. In the Newtonian fluid, both the energy and enstrophy are monotonically decreasing with increasing streamwise wavenumber. In contrast, the Oldroyd-B results show peaks in the energy and enstrophy spectra at $k \sim 1$. The peak in the energy spectral density is enhanced with increasing W.

https://doi.org/10.1017/jfm.2016.455 Published online by Cambridge University Press

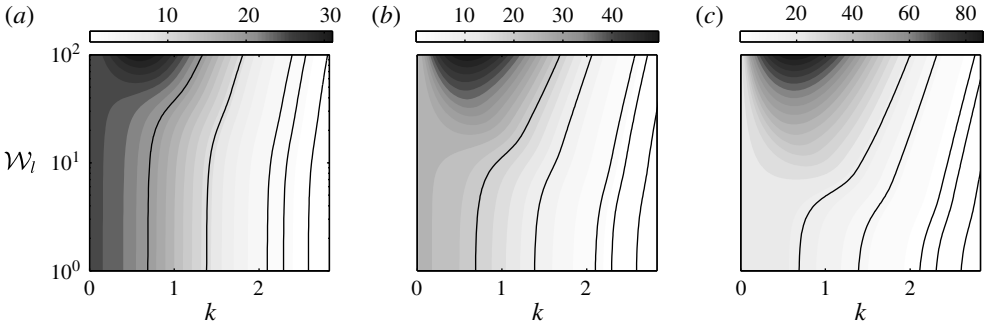


FIGURE 14. Streamwise enstrophy spectra for a shallow-elastic channel with $\alpha_l = 0.5$, while $\mathcal{W}_l$ is varied. Here $R = 1$ and (*a*) $\beta = 0.8$; (*b*) $\beta = 0.5$; (*c*) $\beta = 0.2$. The solid lines identify the contour levels {1, 2, 3, 10, 20}.

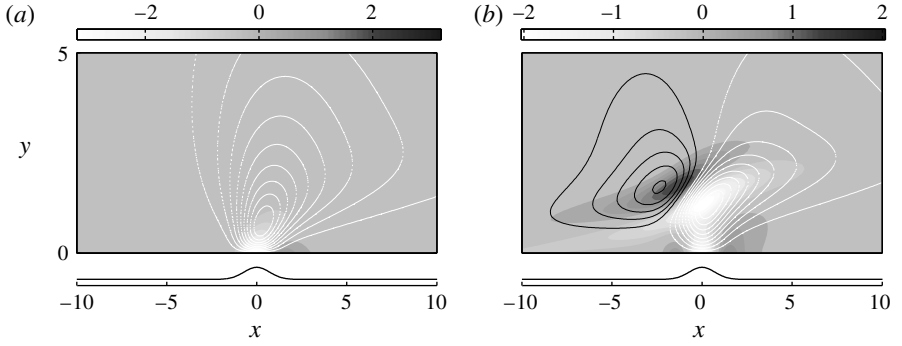


FIGURE 15. Vortical perturbations (top) induced by Gaussian wall bump (bottom) in a deep channel with $\alpha_l = 10$. Filled contours are the spanwise vorticity, lines are the streamfunction. (*a*) Newtonian flow with $R = 1000$. (*b*) Viscoelastic flow with $\Sigma_l = 1.73$ with $\beta = 0.5$, $W = 30$, $R = 1000$.

These results can be understood in the context of our earlier analysis of the shallow-elastic regime. It was demonstrated that, for long waves, a significant amplification of the vorticity at the upper wall was possible provided that $\mathcal{W} \equiv k^* U_0 \varsigma \gg 1$. In those cases, the bulk flow response was shown to be 'elastic' with a constant vorticity, while a large vorticity disturbance was generated at the upper wall due to rapid adjustment in a solvent boundary layer to satisfy the no-slip condition. This is consistent with the present results for the localized disturbance, where enstrophy amplification is most pronounced in long waves, $1/k \gtrsim \alpha_l$. Further evidence is provided in figure 14 where contours of streamwise enstrophy spectra are provided for varying $\mathcal{W}_l \equiv \alpha_l W$. Significant amplification is limited to modes with a local $k\mathcal{W}_l \gg 1$, consistent with our expectation from the monochromatic wall oscillation. The upper wall vorticity generation is increasingly effective as the solvent viscosity is reduced.

The flow response to a Gaussian wall bump in a deep channel is reported in figure 15 for both a Newtonian and an Oldroyd-B fluid. In the Newtonian case a patch of negative spanwise vorticity is generated directly above the bump, with a weaker region of positive vorticity downstream. The vorticity field is tipped forward

https://doi.org/10.1017/jfm.2016.455 Published online by Cambridge University Press

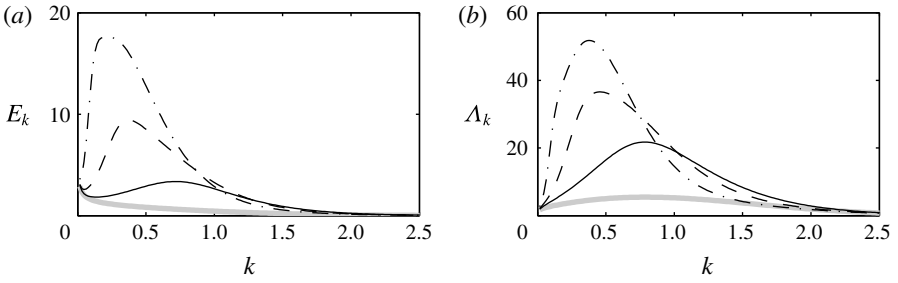


FIGURE 16. Streamwise energy (a) and enstrophy (b) spectra in a deep channel with $\alpha_l = 10$. Here $R = 1000$, $\beta = 0.5$. Grey solid line, Newtonian flow; black solid line, $W = 15$; dashed line, $W = 30$; dot-dashed line, $W = 60$.

with the shear due to the strong inertial effects, $\theta_l \equiv (\alpha_l^2/R)^{1/3} < 1$, and the flow lies in the 'inviscid regime' according to the criteria by Charru & Hinch (2000). This vorticity disturbance, while localized at the wall, induces a much larger scale potential flow. The vorticity field in the viscoelastic case is strikingly different and is dominated by non-local effects: in addition to a response at the wall, there is a significant amplification of vorticity at the critical layer, $y = \Sigma_l$, where the vorticity is arranged in stripes of opposite signs. This non-local vorticity, generated by the kinematic torque amplification mechanism examined in § 4.3, drives the formation of an upstream vortex with opposite circulation. The proximity of the critical layer to the wall allows us to classify the flow as 'transcritical' using the terminology developed in § 3.2.

In figure 16 the influence of elasticity on the streamwise energy and enstrophy spectra is examined for deep channels with a fixed bulk Reynolds number. The Newtonian flow shows a monotonic decay in the spectral energy density with increasing streamwise wavenumber, while the enstrophy peaks at $k \sim 1$. At moderate Weissenberg number ($W = 15$) there is amplification in both energy and enstrophy across the range of streamwise wavenumbers well beyond the levels recorded for the Newtonian reference case. As the Weissenberg number is increased, the energy and enstrophy in the low wavenumbers are enhanced appreciably while being slightly attenuated for larger values of k. These results can be explained by considering the height of the critical layer of each constituent wavelength in the Fourier decomposition of the Gaussian bump. This connection is explored further in figure 17, where contours of the streamwise enstrophy are reported for three deep flows ($\alpha_l = 10$) with $W = \{15, 30, 60\}$. The bulk Reynolds number is varied to change the critical layer height, $y = \Sigma_l$. All three flows show peaks in their enstrophy spectra around $k \sim 1$ when $\Sigma_l \sim 1$, where the vorticity response to the bump shows a strong amplification at the critical layer. As Σ_l increases, enstrophy in the higher wavenumbers is attenuated first, similar to the behaviour reported in figure 16, before the spectra in all three cases reach a similar state as $\Sigma_l \to \infty$. This phenomenon can be interpreted in terms of a transition between 'transcritical' and 'deep-elastic' regimes: in the Fourier decomposition, each constituent wavenumber has its own critical layer. These critical layers all lie at the same dimensional y^* location, but their normalized height relative to each individual wavelength, Σ, increases linearly with k. For a particular choice of Σ_l, part of the spectrum will be transcritical, while above a critical $k \gtrsim \Sigma_l$, the waves can be classified as deep elastic. Therefore, as Σ_l increases, more of the bump's spectrum can be classified as deep elastic and is unable to generate vorticity using

https://doi.org/10.1017/jfm.2016.455 Published online by Cambridge University Press

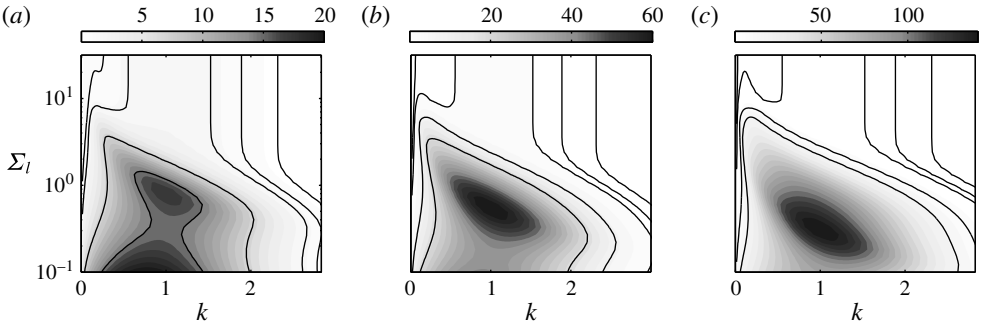


FIGURE 17. Streamwise enstrophy spectra for a deep channel with $\alpha_l = 10$, while Σ_l is varied. Here $\beta = 0.5$ and (*a*) $W = 15$; (*b*) $W = 30$; (*c*) $W = 60$. The solid lines identify the contour levels {1, 2, 3, 10, 20}.

the transcritical amplification mechanism. When Σ_l crosses a threshold value, the entire spectrum is no longer influenced by the critical layer and the perturbation field achieves the same state regardless of the Weissenberg number or solvent viscosity.

In summary, the results for the localized bump display evidence of the three regimes examined in detail in § 4. Whether the dominant behaviour is shallow elastic, transcritical or deep elastic depends on both the normalized channel height, α_l, and the critical layer height relative to the bump length scale, Σ_l. For localized bumps in the shallow-elastic regime, $\alpha_l < 1$, $\Sigma_l > \alpha_l$, a second vortex of opposite sign is generated upstream of the bump by the large vorticity in the upper wall solvent boundary layer. For transcritical flows, vorticity is generated at the critical layer through the kinematic torque amplification mechanism, and the perturbation flow takes the form of a pair of counter-rotating vortices. Both of these behaviours contrast with the Newtonian flows, where a single vortex forms directly above the bump. Note that the interesting phenomenology reported in these computations is most pronounced at high values of the Weissenberg number, W. Therefore, it is important to examine the impact of finite polymer extensibility on vorticity penetration into the flow.

5.2. *The effect of finite extensibility*

As was remarked in § 2, Oldroyd-B fluids model the dissolved polymer chains as infinitely extensible dumbbells, and this simplification can generate unphysical behaviour. Perhaps the most well-known failure of the Oldroyd-B model is its prediction of infinite stresses in extensional flows. Therefore, it is important to verify that the behaviours examined in this work are relevant when the finite extensibility of the polymer is taken into account. In this section, the influence of a wall bump on viscoelastic FENE-P fluid is evaluated numerically in order to assess whether the same regimes reported in § 5.1 remain relevant when the polymer extensibility is finite.

The FENE-P model replaces the Hookean dumbbells of the Oldroyd-B fluid with nonlinear springs (Bird *et al.* 1987),

$$T^*_{ij} = \frac{1}{\varsigma}(FC_{ij} - \delta_{ij}), \tag{5.3a}$$

where

$$F = \frac{L^2 - 3}{L^2 - C_{kk}}, \tag{5.3b}$$

https://doi.org/10.1017/jfm.2016.455 Published online by Cambridge University Press

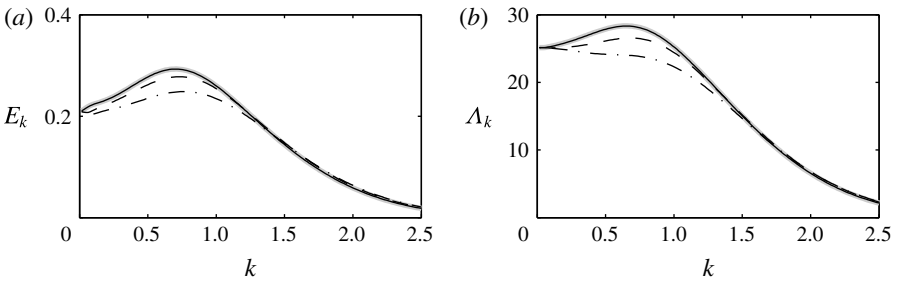


FIGURE 18. Streamwise energy (a) and enstrophy (b) spectra in a FENE-P fluid with $\alpha_l = 0.5$, $R = 1$, $W = 40$, $\beta = 0.5$. Grey solid line, Oldroyd-B; black solid line, $L = 1000$; dashed line, $L = 100$; dot-dashed line, $L = 50$.

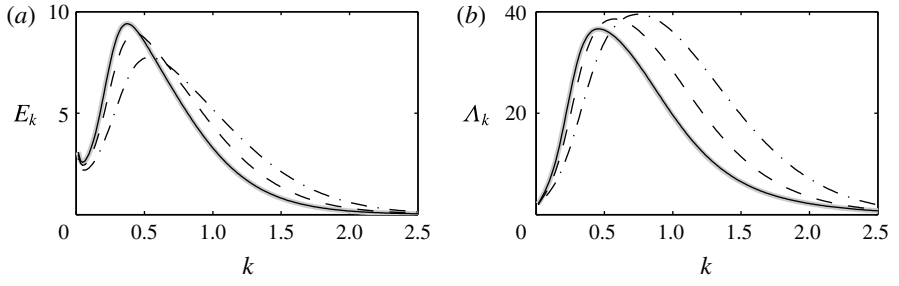


FIGURE 19. Streamwise energy (a) and enstrophy (b) spectra in a FENE-P fluid with $\alpha_l = 10$, $R = 1000$, $W = 30$, $\beta = 0.5$. Grey solid line, Oldroyd-B; black solid line, $L = 1000$; dashed line, $L = 100$; dot-dashed line, $L = 50$.

is the Peterlin function and L is related to the maximum extensibility of the polymer chains $L^2 = L^2_{max} + 3$. In the present configuration, the nonlinear-spring law influences the perturbation field in two ways: (i) a weakening of the base-state normal stress as W/L increases (see appendix B) and (ii) a new form of stress perturbation,

$$\tau^*_{ij} = \frac{F}{\varsigma}\left(c_{ij} + \underbrace{\frac{1}{L^2 - C_{ll}} C_{ij} c_{kk}}_{\mathcal{N}}\right), \tag{5.4}$$

which is labelled $\mathcal{N}$. The full perturbation equations for the FENE-P fluid are provided in appendix B.

Streamwise energy and enstrophy spectra for the FENE-P fluid are reported in figures 18 and 19 for a shallow and a deep channel respectively. Note that the parameter sets correspond to the Oldroyd-B cases considered in figures 13 and 16. For the largest extensibility, $L = 1000$, the results are indistinguishable from the Oldroyd-B cases. For the more realistic values, $L = \{50, 100\}$, the FENE-P results exhibit the same qualitative trends as the Oldroyd-B fluids. In the shallow-elastic flow (figure 18) the energy and enstrophy are damped slightly across the full range of wavenumbers. In the transcritical flow (figure 19), the kinematic amplification mechanism remains active across a band of wavenumbers. The spectra are similar in shape to the Oldroyd-B results, although the peak in both the energy and enstrophy spectra is shifted to higher wavenumbers.

https://doi.org/10.1017/jfm.2016.455 Published online by Cambridge University Press

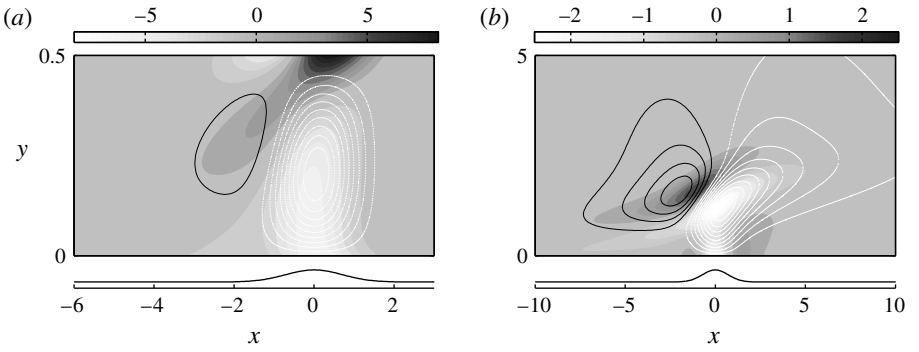


FIGURE 20. Vortical perturbations (top) induced by Gaussian wall bump (bottom) in a FENE-P channels with $L = 100$. Filled contours are the spanwise vorticity, lines are the streamfunction. (*a*) $\alpha_l = 0.5$ with $\beta = 0.5$, $W = 40$, $R = 1$. (*b*) $\alpha_l = 10$ with $\beta = 0.5$, $W = 30$, $R = 1000$.

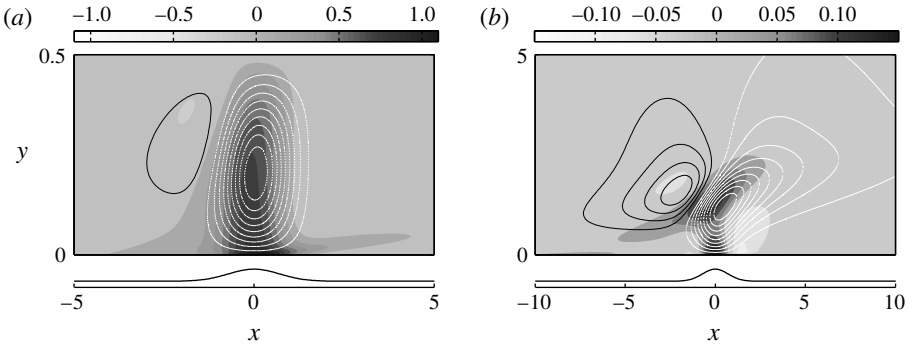


FIGURE 21. Contours of polymer stretch perturbations, c_{kk}/L^2, in Couette flow of a FENE-P fluid with $L = 100$. (*a*) Shallow channel with $\alpha_l = 0.5$, $W = 40$, $R = 1$, $\beta = 0.5$. (*b*) Deep channel with $\alpha_l = 10$, $W = 30$, $R = 1000$, $\beta = 0.5$. Lines are contours of the streamfunction.

In figure 20 the flow response to the Gaussian bump is reported for the flows examined in figures 18 and 19 for the realistic value $L = 100$. The important flow features from the Oldroyd-B results remain: in the shallow-elastic channel, the vorticity maximum is located at the upper wall and a weak secondary vortex is formed upstream of the bump. In the transcritical channel, there is a strong non-local response in the vorticity at the critical layer, which takes the form of stripes tipped forward with the shear.

Finally, the polymer stretch field associated with each flow is examined in figure 21. In the shallow-elastic flow, the polymer is most strongly stretched directly above the wall bump, while a small 'jet' of polymer stretch protrudes downstream along the lower wall. For the transcritical flow, the polymer is stretched in a thin region between the two induced vortices, as anticipated from the vorticity field.

6. Conclusion

The flow response to surface waviness in a viscoelastic Couette flow was examined using linear theory. For an Oldroyd-B fluid at high Weissenberg number, the induced

https://doi.org/10.1017/jfm.2016.455 Published online by Cambridge University Press

vorticity perturbations can be classified using a phase diagram in a similar manner to the Newtonian problem (Charru & Hinch 2000). The viscoelastic phase diagram is parameterized by two quantities: the ratios of the channel depth and of the critical layer height to the length scale of the surface undulation, $\alpha \equiv k^* d$ and $\Sigma \equiv k^* \sqrt{2\nu_p \varsigma}$.

The phase diagram was divided in three regions: (i) when $\alpha < 1$ and $\Sigma > \alpha$, the flow is termed 'shallow elastic'; the surface waves are long relative to the channel depth and the critical layer is outside of the flow domain. The bulk flow response is a constant vorticity generated by a distortion of the highly tensioned mean-flow streamlines. There is a substantial spanwise vorticity generated in a solvent boundary layer at the top wall where the flow adjusts to satisfy the top boundary conditions. (ii) When $\alpha > 1$ and $\Sigma \gtrsim 1$, the flow is labelled 'deep elastic'; neither the top wall or the critical layer influence the perturbation field. The vortical perturbations are not affected by the elasticity in this regime. (iii) When $\alpha > \Sigma$ and $\Sigma \lesssim 1$, the critical layer is inside the flow domain, and lies within one wavelength from the lower wall. This behaviour is termed 'transcritical', and is characterized by generation of vorticity at the critical layer, which is driven by a kinematic amplification mechanism for the polymer torque.

The analysis of a single wall wavelength was followed by a computational study of the flow response to localized disturbances using Fourier superposition. In shallow-elastic flows, the large vorticity generated at the upper wall leads to the formation of a second vortex upstream of the bump. In deep channels a significant vorticity is generated at the critical layer, and this has attached an associate pair of counter-rotating vortices. Calculations of the flow response to isolated bumps using the more realistic FENE-P model showed the same qualitative behaviour in both shallow and deep channels.

Future work should extend the analysis to finite-amplitude wall roughness, where the secondary instability of the curved streamlines in shallow channels may present a pathway to elastic turbulence. The influence of wall undulations on drag-reduced turbulent flows at high Reynolds numbers is also of interest since, in that regime, critical layers can be established in close proximity to the lower wall.

Acknowledgement

This work is sponsored by the Engineering and Physical Sciences Research Council and by the National Science Foundation under grant no. 1511937.

Appendix A. Further details on the transcritical regime

A.1. *Solution of the elastic-Rayleigh equation*

In the bulk of the channel, the streamfunction satisfies the elastic-Rayleigh equation,

$$\frac{\mathrm{d}^2}{\mathrm{d}y^2}\left(\frac{\psi_0}{y}\right) + \frac{2y}{(y^2-\Sigma^2)}\frac{\mathrm{d}}{\mathrm{d}y}\left(\frac{\psi_0}{y}\right) - k^2\left(\frac{\psi_0}{y}\right) = 0. \tag{A 1}$$

A solution is sought in the form of a Frobenius series about $y = \Sigma$ (Bender & Orszag 1978) and takes the form,

$$\psi_0^{\pm}(y) = A_0^{\pm} y \sum_{j=0}^{\infty} b_j (y-\Sigma)^j + B_0^{\pm} y \left(\sum_{j=1}^{\infty} c_j (y-\Sigma)^j + \sum_{j=0}^{\infty} b_j (y-\Sigma)^j \log(y-\Sigma) \right). \tag{A 2}$$

https://doi.org/10.1017/jfm.2016.455 Published online by Cambridge University Press

The branch of the logarithm for $\psi_0^-(y)$ is chosen as $\log(y-\Sigma)=\log|y-\Sigma|-\mathrm{i}\pi$. The series coefficients in (A 2) are

$$\left.\begin{aligned} b_1&=0,\\ b_2&=\frac{k^2 b_0}{4},\\ b_{j\geqslant 3}&=-\frac{(j-1)b_{j-1}}{2\Sigma j}+\frac{k^2 b_{j-2}}{j^2}+\frac{k^2 b_{j-3}}{2\Sigma j^2},\\ c_1&=-\frac{b_0}{2\Sigma},\\ c_2&=-b_2-\frac{c_1}{4\Sigma},\\ c_{j\geqslant 3}&=-\frac{2b_j}{j}-\frac{(2j-1)b_{j-1}}{2\Sigma j^2}-\frac{(j-1)c_{j-1}}{2\Sigma j}+\frac{k^2 c_{j-2}}{j^2}+\frac{k^2 c_{j-3}}{2\Sigma j^2}, \end{aligned}\right\} \tag{A 3}$$

where $b_0=1$ and $c_0=0$.

Close to the critical layer the solution (A 2) is expressed in terms of the critical layer coordinate $\eta\equiv(y-\Sigma)/\delta_c$ and the leading terms are,

$$\psi_0^+(\eta)\sim A_0^+\Sigma+B_0^+\Sigma(\log|\eta|+\log\delta_c)+O(\delta_c), \tag{A 4a}$$

$$\psi_0^-(\eta)\sim A_0^-\Sigma+B_0^-\Sigma(\log|\eta|-\mathrm{i}\pi+\log\delta_c)+O(\delta_c). \tag{A 4b}$$

This suggests an inner expansion

$$\overline{\psi}(\eta)=\log\delta_c\overline{\psi}_{-1}(\eta)+\overline{\psi}_0(\eta)+\cdots. \tag{A 5}$$

The equations satisfied by the inner variable $\overline{\psi}(\eta)=\psi(y)$ are solved below.

A.2. *Solution in the critical layer*

In the critical layer the balance between advection, polymer force generated by T_{11} and solvent diffusion leads to

$$\frac{\mathrm{d}^4\overline{\psi}_i}{\mathrm{d}\eta^4}-\frac{\mathrm{d}}{\mathrm{d}\eta}\left(\mathrm{i}\eta\frac{\mathrm{d}\overline{\psi}_i}{\mathrm{d}\eta}\right)=0, \tag{A 6}$$

where $\eta\equiv(y-\Sigma)/\delta_c(\varepsilon)$ is the shifted coordinate scaled by the viscous length scale in the solvent, $\delta_c=(\varepsilon\beta\Sigma^2/4\dot{\gamma}k(1-\beta))^{1/3}$. Note that this equation is satisfied by the $O(\log\delta_c)$ eigensolution, $\overline{\psi}_{-1}(\eta)$ and the $O(1)$ component, $\overline{\psi}_0(\eta)$. Solutions are sought in the form of Laplace contour integrals,

$$\overline{\psi}_i(\eta)=\int_C f(\zeta)\mathrm{e}^{\eta\zeta}\,\mathrm{d}\zeta, \tag{A 7}$$

where C is a yet unspecified contour in the complex-ζ plane.

Substituting (A 7) into (A 6) and differentiating under the integral sign,

$$\int_C(\zeta^4-\mathrm{i}\eta\zeta^2-\mathrm{i}\zeta)f(\zeta)\mathrm{e}^{\eta\zeta}\,\mathrm{d}\zeta=0. \tag{A 8}$$

https://doi.org/10.1017/jfm.2016.455 Published online by Cambridge University Press

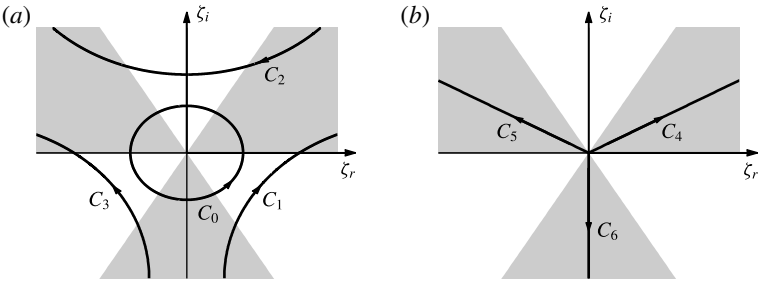


FIGURE 22. Possible integration contours in the complex ζ-plane that define the linearly independent solutions of (A 6).

Integrating by parts yields,

$$\int_C \left[\left(\zeta^4 + \mathrm{i}\zeta\right) f + \mathrm{i}\zeta^2 \frac{\mathrm{d}f}{\mathrm{d}\zeta} \right] \mathrm{d}\zeta - \underbrace{\mathrm{i}\zeta^2 f(\zeta) \mathrm{e}^{\eta\zeta} \Big|_C} = 0, \tag{A 9}$$

where the term identified with an underbrace is evaluated at the end points of the contour. After solving for $f(\zeta)$, linearly independent solutions for the streamfunction are

$$\overline{\psi}_i^j(\eta) = \int_{C_j} \left(\frac{1}{\zeta}\right) \exp\left(\frac{\mathrm{i}\zeta^3}{3} + \eta\zeta\right) \mathrm{d}\zeta, \tag{A 10}$$

where the contours C_j must satisfy

$$\zeta \exp\left(\frac{\mathrm{i}\zeta^3}{3} + \eta\zeta\right) \Big|_{C_j} = 0. \tag{A 11}$$

Valid integration contours are illustrated in figure 22. Contours can encircle the origin. They may also start and end at the origin or in one of the sectors in which $\exp(\mathrm{i}\zeta^3/3)$ is decaying at $\zeta \to \infty$, which are indicated in grey in figure 22. Each contour yields a solution of (A 6), but four contours may not be chosen arbitrarily. For example, contours C_0, C_1, C_2 and C_3 do not produce four independent solutions, since C_1, C_2 and C_3 can be joined at infinity to produce C_0.

Numerically satisfactory solutions can be constructed using integration contours C_i; $i \in [0, 4, 5, 6]$. The integration around C_0 encloses a simple pole, and the solution is a constant. The other paths are parameterized with $\zeta = s\mathrm{e}^{\mathrm{i}\theta}$, with $\theta = \{\pi/6, 5\pi/6, 3\pi/2\}$. The solution is therefore

$$\begin{aligned} \overline{\psi}_i(\eta) \;=\; & \overline{A}_i + \overline{B}_i \int_\sigma^\infty \left(\frac{1}{s}\right) \exp\left(-\frac{s^3}{3} - \mathrm{i}s\eta\right) \mathrm{d}s \\ & + \overline{C}_i \int_\sigma^\infty \left(\frac{1}{s}\right) \exp\left(-\frac{s^3}{3} + \frac{s\eta(\sqrt{3}+\mathrm{i})}{2}\right) \mathrm{d}s \\ & + \overline{D}_i \int_\sigma^\infty \left(\frac{1}{s}\right) \exp\left(-\frac{s^3}{3} + \frac{s\eta(-\sqrt{3}+\mathrm{i})}{2}\right) \mathrm{d}s. \end{aligned} \tag{A 12}$$

https://doi.org/10.1017/jfm.2016.455 Published online by Cambridge University Press

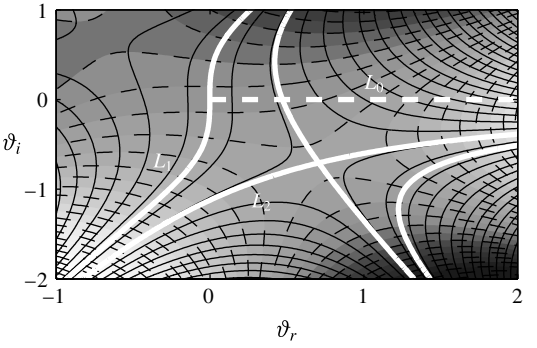


FIGURE 23. Contours of the altitude $\mathscr{A}$ (colours and dashed lines) and phase $\mathscr{P}$ (solid lines) of the function $g(\vartheta)$. The original integration contour, L_0, is identified with the white dashed line. The solid white lines are those on which the phase $\mathscr{P} = -\sigma\lambda^{-1/3}$ and $\mathscr{P} = -\sqrt{2}/3$ and the labels L_1 and L_2 identify the path of steepest descent.

These expressions are valid in the limit $\sigma \to 0$. This limit results in divergent integrals in (A 12). The constant $\overline{A}_i$ can eliminate this effect, and this becomes apparent when (A 12) is matched to the elastic-Rayleigh equation below. For now, the dependence on σ is retained, and the limit $\sigma \to 0$ will be taken once the unknown constants have been determined.

A.3. *Matching with the elastic-Rayleigh equation*

Discarding solutions which are exponentially growing as $\eta \to \pm\infty$, the critical layer streamfunction is,

$$\overline{\psi}_i(\eta) = \overline{A}_i + \overline{B}_i \int_\sigma^\infty \left(\frac{1}{s}\right) \exp\left(-\frac{s^3}{3} - \mathrm{i}s\eta\right) \mathrm{d}s. \tag{A 13}$$

In order to match this expression to the elastic-Rayleigh solutions in the bulk of the channel we examine the integral in the limits $\eta \to \pm\infty$. Here we provide details of the limit $\eta \to \infty$.

The integral in (A 13) is highly oscillatory as $\eta \to \infty$. In order to obtain approximate expressions in this limit we use the method of steepest descent and deform the integration contour so that the phase in the exponent is constant (Bender & Orszag 1978). The dominant contributions to the integral in the limit $\eta \to \infty$ then come from regions of maximum altitude or saddle points.

The exponent in the integral in (A 13) has moveable saddle points in the complex s-plane. Therefore, the change of variable $s = \sqrt{\eta}\vartheta$ is adopted. The integral to be approximated may then be written

$$I(\lambda) = \int_{\sigma\lambda^{-1/3}}^\infty \frac{\mathrm{e}^{\lambda g(\vartheta)}\mathrm{d}\vartheta}{\vartheta}, \tag{A 14}$$

where $\lambda \equiv \eta^{3/2}$ and $g(\vartheta) = -\vartheta^3/3 - \mathrm{i}\vartheta$.

Contours of both the altitude, $\mathscr{A}(\vartheta) \equiv \mathrm{Re}(g(\vartheta))$, and phase, $\mathscr{P}(\vartheta) \equiv \mathrm{Im}(g(\vartheta))$, are plotted in figure 23 in the complex-ϑ plane. The original integration contour, L_0, is along the real axis. The contour is deformed such onto $L_1 + L_2$, along each of which

https://doi.org/10.1017/jfm.2016.455 Published online by Cambridge University Press

$\mathscr{P} = \text{constant}$. The steepest descent paths L_1 and L_2 meet as $\vartheta \to \infty$. Along L_1 the phase $\mathscr{P} = -\sigma\lambda^{-1/3}$, while along L_2 the phase $\mathscr{P} = -\sqrt{2}/3$.

The dominant contributions to the integral $I(\lambda)$ as $\lambda \to \infty$ are from the saddle point on L_2 and the end point $\vartheta = \sigma\lambda^{-1/3}$ on L_1, which is the point of maximum altitude. The contribution from the saddle point is exponentially small in comparison to the end point contribution, and is not presented here. At the end point the path, L_1 is parameterized, $\vartheta - \sigma\lambda^{-1/3} = r\mathrm{e}^{\mathrm{i}\theta}$. As $\lambda \to \infty$ the exponent $g(\vartheta)$ may thus be approximated,

$$\begin{aligned} g(\vartheta) &\approx -\frac{\sigma^3}{3\lambda} - \frac{\mathrm{i}\sigma}{\lambda^{1/3}} + \left(-\frac{\sigma^2}{\lambda^{2/3}} - \mathrm{i}\right) r\mathrm{e}^{\mathrm{i}\theta} + \cdots, \\ &\approx -r - \frac{\mathrm{i}\sigma}{\lambda^{1/3}}. \end{aligned} \tag{A 15}$$

The approximation to $I(\lambda)$ is therefore,

$$\begin{aligned} I(\lambda) = \int_{\sigma\lambda^{-1/3}}^{\infty} \frac{\mathrm{e}^{\lambda g(\vartheta)}\mathrm{d}\vartheta}{\vartheta} &\approx \int_{L_1} \frac{\mathrm{e}^{\lambda g(\vartheta)}\mathrm{d}\vartheta}{\vartheta}, \\ &\approx \int_0^{\infty} \frac{\exp(-\lambda(r + \mathrm{i}\sigma\lambda^{-1/3}))}{r + \mathrm{i}\sigma\lambda^{-1/3}}\,\mathrm{d}r. \end{aligned} \tag{A 16}$$

With a change of variable this expression can be written as a generalized exponential integral (Abramowitz & Stegun 1964),

$$\begin{aligned} I(\lambda) &\approx \int_{\mathrm{i}\sigma\eta}^{\infty} \frac{\mathrm{e}^{-w}\,\mathrm{d}w}{w}, \\ &= E_1(\mathrm{i}\sigma\eta) = -\gamma - \frac{\mathrm{i}\pi}{2} - \log\sigma - \log|\eta| - \sum_{j=1}^{\infty} \frac{(-1)^j(\mathrm{i}\sigma\eta)^j}{jj!}, \end{aligned} \tag{A 17}$$

where $\gamma = 0.5772\ldots$ is the Euler–Mascheroni constant. In the limit $\sigma \to 0$ the algebraic contribution can be ignored and the streamfunction as $\eta \to \infty$ is

$$\overline{\psi}_i(\eta \to \infty) \sim \overline{A}_i + \overline{B}_i \left(-\gamma - \frac{\mathrm{i}\pi}{2} - \log\sigma - \log|\eta|\right). \tag{A 18a}$$

Similar considerations as $\eta \to -\infty$ result in

$$\overline{\psi}_i(\eta \to -\infty) \sim \overline{A}_i + \overline{B}_i \left(-\gamma + \frac{\mathrm{i}\pi}{2} - \log\sigma - \log|\eta|\right). \tag{A 18b}$$

Matching these expressions to inner limit of the elastic-Rayleigh solutions (A 4) reveals $A_0^+ = A_0^- \equiv A_0$, $B_0^+ = B_0^- \equiv B_0$ and determines the constants for the inner solution,

$$\begin{aligned} \overline{\psi}(\eta) &= \Sigma B_0 \log\delta_c + \Sigma A_0 + \Sigma B_0 \left(-\gamma - \frac{\mathrm{i}\pi}{2} - \log\sigma\right) \\ &\quad - \Sigma B_0 \int_{\sigma}^{\infty} \left(\frac{1}{s}\right) \exp\left(-\frac{s^3}{3} - \mathrm{i}s\eta\right) \mathrm{d}s. \end{aligned} \tag{A 19}$$

In the limit $\sigma \to 0$ the logarithmic term regularizes the lower limit of the integral.

https://doi.org/10.1017/jfm.2016.455 Published online by Cambridge University Press

Appendix B. Flow equations for a FENE-P fluid

B.1. *Base state*

In a FENE-P fluid the polymer stress is related to the conformation tensor through a nonlinear-spring law,

$$T_{ij} = \frac{1}{W}(FC_{ij} - \delta_{ij}), \tag{B 1}$$

where F is the Peterlin function,

$$F = \frac{L^2 - 3}{L^2 - C_{kk}}. \tag{B 2}$$

In simple shear, $U = \dot{\gamma} y$, the base-state polymer stresses for a FENE-P fluid can be related to the Oldroyd-B values (Sureshkumar, Beris & Handler 1997),

$$\frac{T_{11}}{T_{11}^{\infty}} = \frac{1}{F^2}, \quad \frac{T_{12}}{T_{12}^{\infty}} = \frac{1}{F}, \tag{B 3a,b}$$

where the superscript ∞ identifies the Oldroyd-B result. The Peterlin function depends on the parameter $\varrho \equiv \dot{\gamma} W/L$,

$$F(\varrho) = \frac{\sqrt{6}\varrho}{2\sinh(q/3)}, \quad \text{with } q = \sinh^{-1}(3\sqrt{6}\varrho/2). \tag{B 4}$$

The function F is monotonically decreasing with increasing ϱ (Ray & Zaki 2014). Therefore, the polymer stresses are always attenuated by finite extensibility. For the parameters of interest in this paper, $\varrho = O(1)$ and the Oldroyd-B scaling remains, $T_{11} = O(W\dot{\gamma}^2)$, $T_{12} = O(\dot{\gamma})$ (Page & Zaki 2015).

B.2. *Linear perturbation equations*

The continuity and momentum equations are,

$$\mathrm{i}ku + \frac{\mathrm{d}v}{\mathrm{d}y} = 0, \tag{B 5a}$$

$$\mathrm{i}k\dot{\gamma} yu + \dot{\gamma} v = -\mathrm{i}kp + \frac{\alpha^2}{R}\left[\beta\left(\frac{\mathrm{d}^2}{\mathrm{d}y^2} - k^2\right)u + (1-\beta)\left(\mathrm{i}k\tau_{11} + \frac{\mathrm{d}\tau_{12}}{\mathrm{d}y}\right)\right], \tag{B 5b}$$

$$\mathrm{i}k\dot{\gamma} yv = -\frac{\mathrm{d}p}{\mathrm{d}y} + \frac{\alpha^2}{R}\left[\beta\left(\frac{\mathrm{d}^2}{\mathrm{d}y^2} - k^2\right)v + (1-\beta)\left(\mathrm{i}k\tau_{12} + \frac{\mathrm{d}\tau_{22}}{\mathrm{d}y}\right)\right]. \tag{B 5c}$$

For a FENE-P fluid, perturbations in the stress are related to stretch perturbations by

$$\tau_{ij} = \frac{F}{W}\left(c_{ij} + \frac{1}{L^2 - C_{ll}}C_{ij}c_{kk}\right). \tag{B 6}$$

The relevant components of the conformation tensor evolve according to,

$$\mathrm{i}k\dot{\gamma} yc_{11} + \frac{1}{W}\tau_{11} = 2\mathrm{i}kC_{11}u + 2C_{12}\frac{\mathrm{d}u}{\mathrm{d}y} + 2\dot{\gamma} c_{12}, \tag{B 7a}$$

$$\mathrm{i}k\dot{\gamma} yc_{12} + \frac{1}{W}\tau_{12} = \mathrm{i}kC_{11}v + C_{22}\frac{\mathrm{d}u}{\mathrm{d}y} + \dot{\gamma} c_{22}, \tag{B 7b}$$

https://doi.org/10.1017/jfm.2016.455 Published online by Cambridge University Press

$$\mathrm{i}k\dot{\gamma}yc_{22} + \frac{1}{W}\tau_{22} = 2\mathrm{i}kC_{12}v + 2C_{22}\frac{\mathrm{d}v}{\mathrm{d}y}, \tag{B 7c}$$

$$\mathrm{i}k\dot{\gamma}yc_{33} + \frac{1}{W}\tau_{33}. \tag{B 7d}$$

REFERENCES

ABRAMOWITZ, M. & STEGUN, I. A. 1964 *Handbook of Mathematical Functions*, 10th edn. Dover.

AGARWAL, A., BRANDT, L. & ZAKI, T. A. 2014 Linear and nonlinear evolution of a localized disturbance in polymeric channel flow. *J. Fluid Mech.* **760**, 278–303.

AHRENS, M., YOO, J. Y. & JOSEPH, D. D. 1987 Hyperbolicity and change of type in the flow of viscoelastic fluids through pipes. *J. Non-Newtonian Fluid Mech.* **24**, 67–83.

AZAIEZ, J. & HOMSY, G. M. 1994 Linear stability of free shear flow of viscoelastic liquids. *J. Fluid Mech.* **268**, 37–69.

BENDER, C. M. & ORSZAG, S. A. 1978 *Advanced Mathematical Methods for Scientists and Engineers*, 1st edn. McGraw-Hill.

BIRD, R. B., ARMSTRONG, R. C. & HASSAGER, O. 1987 *Dynamics of Polymeric Liquids*, 2nd edn. vol. 1. Wiley.

CASANELLAS, L. & ORTÍN, J. 2014 Vortex ring formation in oscillatory pipe flow of wormlike micellar solutions. *J. Rheol.* **58** (1), 149–181.

CHANDRASEKHAR, S. 1961 *Hydrodynamic and Hydromagnetic Stability*. Dover.

CHARRU, F. & HINCH, E. J. 2000 'Phase diagram' of interfacial instabilities in a two-layer Couette flow and mechanism of the long-wave instability. *J. Fluid Mech.* **414**, 195–223.

DENN, M. M. & PORTEOUS, K. C. 1971 Elastic effects in flow of viscoelastic liquids. *Chem. Engng J.* **2**, 280–286.

GORODTSOV, V. A. & LEONOV, A. I. 1967 On a linear instability of a plane parallel Couette flow of viscoelastic fluid. *Z. Angew. Math. Mech. J. Appl. Math. Mech.* **31** (2), 310–319.

GROISMAN, A. & STEINBERG, V. 2000 Elastic turbulence in a polymer solution flow. *Nature* **405**, 53–55.

HODA, N., JOVANOVIĆ, M. R. & KUMAR, S. 2008 Energy amplification in channel flows of viscoelastic fluids. *J. Fluid Mech.* **601**, 407–424.

HODA, N., JOVANOVIĆ, M. R. & KUMAR, S. 2009 Frequency responses of streamwise-constant perturbations in channel flows of Oldroyd-B fluids. *J. Fluid Mech.* **625**, 411–434.

JOSEPH, D. D. 1990 *Fluid Dynamics of Viscoelastic Liquids*. Springer.

JOSEPH, D. D., RENARDY, M. & SAUT, J. C. 1985 Hyperbolicity and change of type in the flow of viscoelastic fluids. *Arch. Rat. Mech. Anal.* **87** (3), 213–227.

JOVANOVIC, M. R. & KUMAR, S. 2010 Transient growth without inertia. *Phys. Fluids* **22**, 023101.

JOVANOVIC, M. R. & KUMAR, S. 2011 Nonmodal amplification of stochastic disturbances in strongly elastic channel flows. *J. Non-Newtonian Fluid Mech.* **166**, 755–778.

LARSON, R. G., SHAQFEH, E. S. G. & MULLER, S. J. 1990 A purely elastic instability in Taylor–Couette flow. *J. Fluid Mech.* **218**, 573–600.

LIEU, B. K., JOVANOVIĆ, M. R. & KUMAR, S. 2013 Worst-case amplification of disturbances in inertialess Couette flow of viscoelastic fluids. *J. Fluid Mech.* **723**, 232–263.

MEULENBROEK, B., STORM, C., MOROZOV, A. N. & VAN SAARLOOS, W. 2004 Weakly nonlinear subcritical instability of visco-elastic Poiseuille flow. *J. Non-Newtonian Fluid Mech.* **116** (2-3), 235–268.

MOROZOV, A. & SAARLOOS, W. V. 2005 Subcritical finite-amplitude solutions for plane couette flow of viscoelastic fluids. *Phys. Rev. Lett.* **95** (2), 1–4.

MOROZOV, A. N. & SAARLOOS, W. V. 2007 An introductory essay on subcritical instabilities and the transition to turbulence in visco-elastic parallel shear flows. *Phys. Rep.* **447**, 112–143.

MULLER, S. J., LARSON, R. G. & SHAQFEH, E. S. G. 1989 A purely elastic transition in Taylor–Couette flow. *Rheol. Acta* **28**, 499–503.

https://doi.org/10.1017/jfm.2016.455 Published online by Cambridge University Press

PAGE, J. & ZAKI, T. A. 2014 Streak evolution in viscoelastic Couette flow. *J. Fluid Mech.* **742**, 520–551.

PAGE, J. & ZAKI, T. A. 2015 The dynamics of spanwise vorticity perturbations in homogeneous viscoelastic shear flow. *J. Fluid Mech.* **777**, 327–363.

PAN, L., MOROZOV, A., WAGNER, C. & ARRATIA, P. E. 2013 Nonlinear elastic instability in channel flows at low Reynolds numbers. *Phys. Rev. Lett.* **110**, 174502.

RALLISON, J. M. & HINCH, E. J. 1995 Instability of a high-speed submerged elastic jet. *J. Fluid Mech.* **288**, 311–324.

RAY, P. K. & ZAKI, T. A. 2014 Absolute instability in viscoelastic mixing layers. *Phys. Fluids* **26** (1), 014103.

RAY, P. K. & ZAKI, T. A. 2015 Absolute/convective instability of planar viscoelastic jets. *Phys. Fluids* **27**, 014110.

RENARDY, M. & RENARDY, Y. 1986 Linear stability of plane Couette flow of an upper convected Maxwell fluid. *J. Non-Newtonian Fluid Mech.* **22** (1), 23–33.

SHAQFEH, E. S. G. 1996 Purely elastic instabilities in viscometric flows. *Annu. Rev. Fluid Mech.* **28**, 129–185.

SHAQFEH, E. S. G., MULLER, S. J. & LARSON, R. G. 1992 The effects of gap width and dilute solution properties on the viscoelastic Taylor–Couette instability. *J. Fluid Mech.* **235**, 285–317.

SURESHKUMAR, R., BERIS, A. N. & HANDLER, R. A. 1997 Direct numerical simulation of the turbulent channel flow of a polymer solution. *Phys. Fluids* **9**, 743–755.

TANNER, R. I. 1962 Note on the Rayleigh problem for a visco-elastic fluid. *Z. Angew. Math. Phys.* **13**, 573–580.

TORRALBA, M., CASTREJÓN-PITA, A. A., HERNÁNDEZ, G., HUELSZ, G., DEL RÍO, J. A. & ORTÍN, J. 2007 Instabilities in the oscillatory flow of a complex fluid. *Phys. Rev.* E **75**, 056307.

YOO, J. Y. & JOSEPH, D. D. 1985 Hyperbolicity and change of type in the flow of viscoelastic fluids through channels. *J. Non-Newtonian Fluid Mech.* **19**, 15–41.

ZHANG, M., LASHGARI, I., ZAKI, T. A. & BRANDT, L. 2013 Linear stability analysis of channel flow of viscoelastic Oldroyd-B and FENE-P fluids. *J. Fluid Mech.* **737**, 249–279.

ZHOU, L., COOK, L. P. & MCKINLEY, G. H. 2012 Multiple shear-banding transitions for a model of wormlike micellar solutions. *SIAM J. Appl. Maths* **72**, 1192–1212.

https://doi.org/10.1017/jfm.2016.455 Published online by Cambridge University Press